bioRxiv preprint doi: https://doi.org/10.1101/2022.06.10.495677; this version posted June 12, 2022. The copyright holder for this preprint (which was not certified by peer review) is the author/funder, who has granted bioRxiv a license to display the preprint in perpetuity. It is made available under aCC-BY-NC-ND 4.0 International license.

The Fc-effector function of COVID-19 convalescent plasma contributes to SARS-CoV-2 treatment efficacy in mice.

Irfan Ullah[1], Guillaume Beaudoin-Bussières[2,3#], Kelly Symmes[1#] Marc Cloutier[4], Eric Ducas[4], Alexandra Tauzin[2,3], Annemarie Laumaea[2,3], Philippe Bégin[5,6], Walther Mothes[7], Priti Kumar[1], Renée Bazin[4], Andrés Finzi[2,3,8], and Pradeep D. Uchil[7*$]

[1]Department of Internal Medicine, Section of Infectious Diseases, Yale University School of Medicine, New Haven, CT 06520, USA

[2]Centre de Recherche du CHUM, Montréal, QC, H2X0A9, Canada

[3]Département de Microbiologie, Infectiologie et Immunologie, Université de Montréal, Montréal, QC, H2X0A9, Canada

[4]Hema-Quebec, Affaires Médicales et Innovation, Québec, QC, G1V 5C3, Canada.

[5]Section of Allergy, Immunology and Rheumatology, Department of Pediatrics, CHU Sainte-Justine, Montréal, Québec, Canada

[6]Department of Médicine, Centre Hospitalier de l'Université de Montréal, Montréal, Québec, Canada

[7]Department of Microbial Pathogenesis, Yale University School of Medicine, New Haven, CT 06510, USA

[8]Department of Microbiologie and Immunologie, McGill Université, Montréal, QC H3A 0G4, Canada.

# Contributed equally

***Corresponding authors:** Priti Kumar: priti.kumar@yale.edu, Renée Bazin: Renee.Bazin@hema-quebec.qc.ca, Andrés Finzi: andres.finzi@umontreal.ca, **$**Pradeep Uchil: pradeep.uchil@yale.edu

bioRxiv preprint doi: https://doi.org/10.1101/2022.06.10.495677; this version posted June 12, 2022. The copyright holder for this preprint (which was not certified by peer review) is the author/funder, who has granted bioRxiv a license to display the preprint in perpetuity. It is made available under aCC-BY-NC-ND 4.0 International license.

[$]**Lead Author**: pradeep.uchil@yale.edu

Main Figures: 7

Supplemental figures: 6

bioRxiv preprint doi: https://doi.org/10.1101/2022.06.10.495677; this version posted June 12, 2022. The copyright holder for this preprint (which was not certified by peer review) is the author/funder, who has granted bioRxiv a license to display the preprint in perpetuity. It is made available under aCC-BY-NC-ND 4.0 International license.

SUMMARY

COVID-19 convalescent plasmas (CCPs) are chosen for plasma therapy based on neutralizing titers and anti-Spike immunoglobulin levels. However, specific CCP characteristics that promote SARS-CoV-2 control in recipients are complex and incompletely defined. Using an *in vivo* imaging approach, we demonstrate that CCPs with low neutralizing and high Fc-effector activity, in contrast to those with poor Fc-function, afford effective prophylaxis and therapy in K18-hACE2 mice lethally challenged with SARS-CoV-2-nLuc. Macrophages and neutrophils significantly contributed to CCP effects during therapy but to a reduced extent under prophylaxis. Both IgG and Ig(M+A) were required during therapy, but the IgG fraction alone was sufficient during prophylaxis. Finally, despite neutralizing poorly, SARS-CoV-2 Wuhan-elicited CCPs delayed Delta and Beta variants of concern (VOC)-induced mortality in mice illustrating the contribution of polyclonal Fc-effector functions in immunity against VOCs. Thus, in addition to neutralization, Fc-effector activity is a significant criterion for CCP selection for therapeutic applications.

Key words: Fc-effector, convalescent plasma, ADCC, COVID-19, neutrophils, macrophages, SARS-CoV-2, IgG, IgM, IgA

bioRxiv preprint doi: https://doi.org/10.1101/2022.06.10.495677; this version posted June 12, 2022. The copyright holder for this preprint (which was not certified by peer review) is the author/funder, who has granted bioRxiv a license to display the preprint in perpetuity. It is made available under aCC-BY-NC-ND 4.0 International license.

Introduction

Convalescent plasma (CP) therapy is a first line of treatment when the human population lacks pathogen-specific immunity and treatment options are limited. CP therapy involves collecting plasma from recovered patients to harness “passive immunity” provided by pathogen-specific antibodies for preventing or treating disease in infected patients (Casadevall and Scharff, 1995). The use of CP therapy dates back to the 1918 influenza pandemic and more recently to fight outbreaks caused by SARS-CoV-1, MERS and Ebola (Cao and Shi, 2020; Luke et al., 2006; Mair-Jenkins et al., 2015). CP therapy may be of particular interest for the aged and immune-suppressed cancer or transplant patients where vaccination fails to elicit protective antibody responses as well as in co-morbid populations where vaccination cannot be used (Beraud et al., 2022; Ljungquist et al., 2022; Pinkus and Said, 1986). Unlike with vaccines and monoclonal antibodies (mAbs), CP therapy requires limited development and standard infrastructure for blood collection and is rapidly deployable globally even under low resource settings. CP is adaptable to emerging SARS-CoV-2 variants of concern (VOCs) when the plasma source is from convalescent human subjects infected with homologous variant virus strains. Additionally, the polyclonal nature of CPs also makes them relatively effective against heterologous variants. In contrast, targeted immune therapies need development from scratch to specifically target newly arising mutations as is currently the case with mRNA vaccines and neutralizing antibody (nAb) cocktails for SARS-CoV-2 Omicron variants and sublineages (Greaney et al., 2022; Tada et al., 2022; Tartof et al., 2022). Therefore, CP therapy remains a rapidly deployable go-to countermeasure for emerging and future pathogens with pandemic potential.

Currently, the choice of COVID-19 convalescent plasma (CCP) for therapy is driven by high titers of anti-SARS-CoV-2 Spike IgG (Median titer: 1:3200) and neutralization titer [inhibitory dilution (ID_{50}] >1:250) (Villa, 2021). Neutralizing antibodies (nAbs) in CCPs can inactivate virus and CCP administration has reduced inflammation and helped mitigate SARS-CoV-2-induced

bioRxiv preprint doi: https://doi.org/10.1101/2022.06.10.495677; this version posted June 12, 2022. The copyright holder for this preprint (which was not certified by peer review) is the author/funder, who has granted bioRxiv a license to display the preprint in perpetuity. It is made available under aCC-BY-NC-ND 4.0 International license.

acute respiratory disorder syndrome (ARDS) (Basheer et al., 2021). Thus, plasma neutralizing titers are a critical correlate of SARS-CoV-2 immunity and undoubtedly an important criterion for the selection of CCP for therapy (Dispinseri et al., 2021). However, the efficacy of CCP therapy has been questioned by large randomized clinical trials (RCTs) such as RECOVERY, CONCOR-1, and REMAP-CAP that found little to no evidence in reducing the risk of intubation or death from administration of high-titer CCP in hospitalized patients (Begin et al., 2021; Writing Committee for the et al., 2021). In the CONCOR-1 trial, higher levels of IgG specific for the membrane-bound Spike with disproportionally low neutralizing and Fc-effector functions were associated with worse outcomes (Begin et al., 2021). Emerging consensus from other RCTs is that if CCP is used, it should contain the highest neutralizing titers possible and be transfused early in the disease course before patients required greater supportive therapies to increase the likelihood of benefit (Korley et al., 2021).

CCPs are complex and contain an ensemble of polyclonal antibodies with different immunoglobulin (Ig) isotypes, epitope specificity, virus-neutralizing and non-neutralizing activities. Despite the presence of beneficial nAbs, the plasma milieu may or may not act in concert to produce the desired antiviral activities required for protection in recipients. Additional signatures of CCP that track with positive outcome are required to better characterize the clinical utility of and choice of CCP for plasma therapy. In addition to directly neutralizing, antibodies can utilize their Fc domain for mediating effector functions by interacting with Fc receptors (FcRs) expressed on innate immune cells (Beaudoin-Bussieres et al., 2022; Ullah et al., 2021; van Erp et al., 2019; Winkler et al., 2021). FcR engagement on neutrophils, monocytes, and natural killer (NK) cells can elicit multiple activities including the clearance of viral particles through phagocytosis (antibody-dependent phagocytosis; ADP) and cytotoxic killing of virus-infected cells (antibody-dependent cellular cytotoxicity; ADCC). However, not all antigen-binding nAbs or non-neutralizing antibodies (non-nAbs) have the ability to stimulate Fc effector functions. A multitude of factors

bioRxiv preprint doi: https://doi.org/10.1101/2022.06.10.495677; this version posted June 12, 2022. The copyright holder for this preprint (which was not certified by peer review) is the author/funder, who has granted bioRxiv a license to display the preprint in perpetuity. It is made available under aCC-BY-NC-ND 4.0 International license.

including epitope specificity, angle of approach, isotype, glycosylation pattern, polymorphism and levels of FcR on innate immune cell type influence activation by antibody-antigen complexes (Lu et al., 2018; Patel et al., 2019; Pereira et al., 2018; Tay et al., 2019). Several studies have now shown that purified monoclonal SAR-CoV-2 nAbs rely on Fc-effector functions for improved *in vivo* efficacy especially during therapy (Schafer et al., 2021; Ullah et al., 2021; Winkler et al., 2021; Yamin et al., 2021). Moreover, introducing Fc-FcγR binding enhancer mutations (GASDALIE) have improved *in vivo* nAb efficacy and reduced dosage (Li et al., 2022; Yamin et al., 2021). 80-96% of Spike-binding antibodies in plasma are non-neutralizers (Jennewein et al., 2021). Given that the predominant proportion of antibodies in plasma are non-nAbs, their contribution to the overall Fc- mediated targeting of SARS-CoV-2 virions and virus-infected cells is expected to be significant. Non-nAbs, through Fc-function, may synergize with nAbs to improve overall efficacies especially in a polyclonal setting like in the plasma (Beaudoin-Bussieres et al., 2022; Tauzin et al., 2021). Furthermore, Fc- functions of antibodies elicited by prior infection or vaccination are a suggested correlate for continued immunity against emerging variants of concerns (VOCs) despite compromised neutralization (Anand et al., 2021; Kaplonek et al., 2022b; Richardson et al., 2022; Tauzin et al., 2021). Thus, given the emerging evidence of Fc-mediated antibody effector functions in both protection and disease caused by SARS-CoV-2, presence of robust Fc-effector activities may serve as an additional criterion for selecting CCPs for therapeutic applications. While the presence of SARS-CoV-2-specific antibodies in CCPs that elicit Fc-mediated effector activity have independently correlated with therapeutic benefits (Begin et al., 2021), direct *in vivo* evidence beyond correlation is lacking.

K18-hACE2 mice are highly susceptible to SARS-CoV-2 infection (Halfmann et al., 2022; McCray et al., 2007; Park et al., 2022; Seehusen et al., 2022; Zheng et al., 2021). They represent a practical and relevant animal model to rapidly navigate through the multiple complex activities of CCP and identify those that contribute to protection, addressing limitations of *in vitro* assay-

bioRxiv preprint doi: https://doi.org/10.1101/2022.06.10.495677; this version posted June 12, 2022. The copyright holder for this preprint (which was not certified by peer review) is the author/funder, who has granted bioRxiv a license to display the preprint in perpetuity. It is made available under aCC-BY-NC-ND 4.0 International license.

driven plasma analyses that cannot predict *in vivo* effects. Here we used the K18-hACE2 mouse model together with bioluminescence imaging for tracking SARS-CoV-2 infection to screen CCPs. Our screen identified a CCP with low neutralizing (ID_{50}<1:250) but robust Fc-effector activity that protected mice from lethal challenge with homologous WA1 strain prophylactically as well as therapeutically. In contrast, CCPs with similarly low neutralizing titers but poor Fc-effector activity did not confer protection. Depletion of macrophages and neutrophils revealed that these innate immune cells contributed significantly to CCP-mediated protection but to a higher extent during therapy than under prophylaxis. Depletion of antibody classes from plasma showed that IgG as well as Ig(M+A) fractions were required for maximal *in vivo* efficacy during therapy. In contrast, the IgG fraction alone sufficed for prophylaxis. IgG- Fc-effector functions were however crucial for prophylaxis in the absence of Ig(M+A). Furthermore, ancestral SARS-CoV-2 (Wuhan)-elicited CCPs delayed mortality by Delta and Beta VOCs despite sub-optimal neutralization demonstrating the importance of polyclonal Fc-effector functions in cross-immunity against VOCs. These data make a compelling case for the relevance of Fc-effector activities when assessing CCP therapeutic potency and suggest that it could potentially serve as an additional criterion for its selection. Our study, in addition to highlighting the versatility of the K18-mouse model in dissecting complex activity mechanisms of CCPs, identifies polyclonal Fc-effector functions as a key CCP profile necessary for the successful treatment of infections by SARS-CoV-2 and VOCs.

Results

Screening in SARS-CoV-2-challenged K18-hACE2 mice allows identification of COVID-19 convalescent plasmas (CCPs) with net protective profiles

We classified CCPs with low nAb titer [inhibitory dilution (ID_{50}) ≤ 250] (Gundlapalli et al., 2021; Villa, 2021) collected during the first wave of COVID-19 based on their *in vitro* ADCC activity **(Figure 1A, B)**. To determine whether Fc activity translates to a protective profile *in vivo*, we

bioRxiv preprint doi: https://doi.org/10.1101/2022.06.10.495677; this version posted June 12, 2022. The copyright holder for this preprint (which was not certified by peer review) is the author/funder, who has granted bioRxiv a license to display the preprint in perpetuity. It is made available under aCC-BY-NC-ND 4.0 International license.

147 analyzed CCPs for their effects in K18-hACE2 mice challenged with homologous SARS-CoV-2
148 WA1 under both prophylactic and therapeutic regimens **(Figure 1C)**. Analyses of body weight
149 loss, N mRNA copy numbers and survival revealed that CCP-6, with the highest ADCC activity *in*
150 *vitro* (%ADCC= 91), prevented body weight loss, controlled virus replication in target organs
151 (nose, lungs and brain) and averted from SARS-CoV-2-induced mortality **(Figure 1D-F)**. Mice
152 treated prophylactically with CCP-3, 4 and 5 with reasonable ADCC activity (%ADCC= 50-60%),
153 lost body weight initially but started recovering by 7 dpi and eventually controlled virus replication
154 in target organs. In contrast, mice that received CCP-1 or CCP-2 with low ADCC activity (11 and
155 16% respectively) did not control virus replication (N mRNA copy numbers) in target organs and
156 succumbed by 6 dpi like the mouse in mock-treated cohort. The importance of Fc function was
157 evident when 3 out of 4 CCPs with ADCC activity also rescued mice from SARS-CoV-2-induced
158 mortality upon administration at 2 dpi after infection was established **(Figure 1G-I)**. To note
159 however, CCP-5, that had the lowest neutralizing activity, did not protect therapeutically despite
160 reasonable Fc activity. Accordingly, polyclonal Fc-effector functions may contribute to protection,
161 but some level of neutralizing activity may be necessary for therapeutic control of established
162 infections. Thus, our data highlights the complexity of plasma milieu-where a single characteristic
163 may not be sufficient to define candidate CCPs for therapy and showcases the utility of *in vivo*
164 screening to identify CCPs with net protective characteristics for an optimal therapeutic outcome.
165
166 **In-depth Analysis of Protective Effects of CCPs With Fc-effector Activity**
167 To better understand the basis for CCP-mediated protection we chose CCP-6 whose protective
168 profile depended on both neutralizing and Fc-effector functions as well as CCP-2 with low ADCC
169 activity (16% vs 91% for CCP-6) as well as low neutralizing activity (1:25 vs 1:160 for CCP-6) for
170 in-depth characterization and bioluminescence imaging (BLI)-based studies **(Figure 2)**. We first
171 prophylactically treated mice (n=7) with CCPs (i.p.) 1 day before intranasal (i.n.) challenge with
172 SARS-CoV-2-nLuc **(Figure 2A-F)**. Temporal BLI imaging and quantification of nLuc signals to

bioRxiv preprint doi: https://doi.org/10.1101/2022.06.10.495677; this version posted June 12, 2022. The copyright holder for this preprint (which was not certified by peer review) is the author/funder, who has granted bioRxiv a license to display the preprint in perpetuity. It is made available under aCC-BY-NC-ND 4.0 International license.

monitor virus replication revealed that prophylaxis with CCP-2 or hIgG1 did not prevent SARS-CoV-2 WA1 nLuc infection and subsequent virus spread **(Figure 2B-D)**. In contrast, CCP-6 prophylaxis completely blocked initiation of virus infection as no detectable nLuc signals were observed in K18-hCE2 mice. These data were corroborated by body weight and survival analyses where isotype-treated control and CCP-2 treated mice steadily lost body weight upon infection and succumbed to infection by 6 dpi while CCP-6-treated mice gained weight indicating complete protection **(Figure 2E-F)**. nLuc signals measured separately in individual isolated target organs after necropsy also corresponded to viral loads (N mRNA expression, viral titers) **(Figure S1A-D)**. In addition, CCP-2 and isotype-treated control cohorts displayed 10-1000-fold induction of inflammatory cytokine mRNA expression in target organs **(Figure S1E-F)**. In contrast, cytokine mRNA expression in CCP-6 treated animals were at basal levels indicating complete protection from SARS-CoV-2 infection.

To confirm the ability of CCP-6 to clear established infection (therapeutic mode), we treated mice 2 days after intranasal (i. n.) challenge with SARS-CoV-2-nLuc **(Figure 2G)**. Quantification of nLuc signals after temporal BLI imaging revealed that therapy with the CCP-2 or hIgG1 did not control expanding SARS-CoV-2 replication in the lungs and allowed virus dissemination into the brain in K18-hACE2 mice **(Figure 2H-J)**. In contrast, mice treated with CCP-6 cleared pre-established infection in the lungs by 8 dpi. Remarkably, despite detectable neuroinvasion at 6 dpi, CCP-6 treatment controlled and subsequently cleared virus in the brain of infected animals by 10 dpi **(Figure 2H-J)**. These data were again corroborated in body weight analyses and survival experiments where CCP-2 and hIgG1-treated mice lost ~20% of their starting body weight and succumbed to infection by 6 dpi while all CCP-6-treated mice survived and regained body weight **(Figure 2K-L)**. A significant decrease in nLuc signal intensity was also seen in individual target tissues (nose, lung brain) post-necropsy in CCP-6 treated mice, which correlated with viral loads as well as mRNA levels of Nucleocapsid (N) and inflammatory cytokines in contrast to hIgG1 and CCP-2-treated cohorts of mice **(Figure S1G-L)**. Altogether, these data confirmed the importance

bioRxiv preprint doi: https://doi.org/10.1101/2022.06.10.495677; this version posted June 12, 2022. The copyright holder for this preprint (which was not certified by peer review) is the author/funder, who has granted bioRxiv a license to display the preprint in perpetuity. It is made available under aCC-BY-NC-ND 4.0 International license.

CCP-6 with robust ADCC activity in conferring protection particularly against established SARS-CoV-2 infection, when CCPs are mainly deployed for therapeutic benefits.

Macrophages and Neutrophils Contribute Marginally to Protection Mediated by CCP in Prophylaxis

CCP potency against SARS-CoV-2 is a result of both neutralizing activity and Fc-mediated mobilization of innate immune cells by antibodies for elimination of virus particles and infected cells. To evaluate involvement of innate immune cells in CCP-6 prophylaxis, we immuno-depleted neutrophils (anti-Ly6G) or macrophages (anti-CSF1R) during CCP-prophylaxis. Flow cytometry confirmed that ~98% neutrophils ($CD45^+CD11b^+Ly6G^+$) in blood or ~75% of lung-resident macrophages ($CD45^+CD11b^+$ $Ly6G^-Ly6C^-CD68^+$) were depleted following treatment with depleting antibodies **(Figure S2A-D)**. Depletion of these innate immune cell types did not alter the susceptibility of K18-hACE2 mice to SARS-CoV-2 infection **(Figure S2E-J)**. BLI analyses revealed transient and weak SARS-CoV-2 replication in the lungs at 4 and 6 dpi that cleared by 10 dpi in CCP-6-treated cohort with immune cell depletion, as determined by the nLuc signal (Flux p/s) **(Figure 3A-C)**. In addition, CCP-6 could still prevent virus dissemination to the brain **(Figure 3D)**. However, a transient body weight loss (up to 10%) in K18-hACE2 mice occurred before complete recovery in contrast to mice that were not depleted of these innate cell types **(Figure 3E, F)**. Post-necropsy analyses (organ flux, tissue viral loads and inflammatory cytokine mRNA expression) also confirmed virological control at the experimental endpoint **(Figure 3G-L)**. However, inflammatory cytokines were significantly higher in the lungs compared to undepleted cohorts. Thus, while the neutralizing activity played a major role during CCP-6 prophylaxis, our data indicate a marginal but distinct contribution of antibody Fc-effector functions in engaging immune cells to control residual infection and mitigating inflammation.

Neutrophils and Macrophages Contribute Significantly to CCP Potency During Therapy

bioRxiv preprint doi: https://doi.org/10.1101/2022.06.10.495677; this version posted June 12, 2022. The copyright holder for this preprint (which was not certified by peer review) is the author/funder, who has granted bioRxiv a license to display the preprint in perpetuity. It is made available under aCC-BY-NC-ND 4.0 International license.

Next, we depleted neutrophils (anti-Ly6G) or macrophages (anti-CSF1R) to analyze the role of innate effector cells toward the therapeutic effects of CCP-6 *in vivo* **(Figure 4A)**. Longitudinal BLI analyses and nLuc signal quantification revealed that depletion of either macrophages or neutrophils significantly compromised CCP-6-mediated virologic control **(Figure 4B-D, Figure S3)**. Innate immune cell-depleted cohorts lost ~20-30 % of their body weight and succumbed to infection **(Figure 4E, F)** with 50% and 100% of mice in macrophage and neutrophil-depleted cohorts respectively underwent a one-day delay in death upon CCP-6 treatment. Virus neuroinvasion occurred in 50 and 75% of mice (respectively) but after a 2-day delay compared to isotype antibody-treated mice (4 vs 6 dpi) reflecting the ability of CCP-6 to prevent virus neuroinvasion upto an extent even in the absence innate cells. These data suggested a more significant contribution of macrophages compared to neutrophils in CCP-6-mediated Fc effector functions during therapy. Innate immune cell depletion compromised CCP-6-mediated virologic control resulting in higher viral loads in the nose and lungs like control cohorts (hIgG1 and rat IgG2A-treated) at experimental endpoints **(Figure 4G)**. The ability of CCP-6 to prevent exacerbated expression of inflammatory cytokine mRNAs (CCL2, CXCL10, IFNG) in the lungs was also significantly compromised when neutrophils or macrophages were depleted **(Figure 4H, I)**. However, inflammatory cytokines (CCL2, CXCL10) in the brain remained under control reflecting the delay in neuroinvasion compared to isotype antibody-treated cohorts **(Figure 4H)**. These data show that Fc-effector functions mediated by innate immune effector cells significantly contributed to CCP-6-mediated protection during therapy and were also required to dampen inflammation especially in the lungs where SARS-CoV-2 established infection.

Polyconal IgGs Contribute to Protection During CCP Prophylaxis

IgM and IgA are mucosal antibodies that function as the first line of defense against mucosal pathogens (Russell et al., 2020). Although not as potent as IgG, multivalent antibodies like IgM (pentamer: decavalent) and IgA (dimer: tetravalent) can exhibit enhanced neutralization due to

bioRxiv preprint doi: https://doi.org/10.1101/2022.06.10.495677; this version posted June 12, 2022. The copyright holder for this preprint (which was not certified by peer review) is the author/funder, who has granted bioRxiv a license to display the preprint in perpetuity. It is made available under aCC-BY-NC-ND 4.0 International license.

their avidity (Gasser et al., 2021; Ku et al., 2021; Wang et al., 2021). We depleted IgG or Ig(M+A) from CCP-6 to evaluate the contribution of specific antibody classes towards protection. We confirmed successful depletion of antibody class-subsets by class-specific Ig ELISA [<99% of IgG or 90-95% of Ig(M+A)] **(Figure S4A)** and flow-cytometric evaluation of Spike-specific isotype content using Spike-expressing HEK293 cells **(Figure S4B)**. ADCC analyses of the undepleted and depleted CCP-6 revealed that *in vitro* Fc- activities predominantly tracked with Ig(M+A)-depleted fraction **(Figure S4C)**. While both fractions displayed SARS-CoV-2 neutralizing activity **(Figure S4D)**, the Ig(M+A) depleted fraction (containing IgG) demonstrated ~2.3-fold higher neutralizing activity than the IgG-depleted-fraction.

We next investigated the anti-SARS-CoV-2 *in vivo* efficacy of class-depleted plasma fractions during prophylaxis **(Figure 5A)**. Unfractionated CCP-6 was diluted before use to account for the loss in IgG (Equalized IgG) in the Ig(M+A)-depleted fraction incurred during the depletion procedure. Longitudinal BLI revealed that IgG-depletion led to a near-complete loss in CCP-6 mediated protection with uncontrolled virus replication, neuroinvasion, 15-20% body weight loss and 100% mortality **(Figure 5B-F, Figure S5A-B)**. In contrast, Ig(M+A)-depleted fraction displayed virologic control like undepleted CCP-6 (Equalized IgG) with 100% survival efficacy **(Figure 5F)** despite a small reduction (<10%) in body weight compared to undepleted plasma **(Figure 5E, F)**. Significantly higher viral loads and inflammatory cytokine mRNA expression in target organs reflected the loss of virologic control in mice treated with IgG-depleted CCP-6 compared to mice treated with unfractionated and Ig(M+A)-depleted plasma **(Figure 5G-I)**. Thus, polyclonal IgGs predominantly contributed to virologic control and protection with marginal but distinct contribution from polyclonal Ig(M+A) during CCP-6 prophylaxis.

To decipher if direct neutralization and/or Fc-mediated innate cell-recruitment contributed to protection during prophylaxis with Ig(M+A)-depleted plasma (containing IgG), we immuno-depleted neutrophils (anti-Ly6G). Interestingly, compared to the undepleted plasma where innate cells contributed marginally during prophylaxis, neutrophil depletion had a significant impact on

bioRxiv preprint doi: https://doi.org/10.1101/2022.06.10.495677; this version posted June 12, 2022. The copyright holder for this preprint (which was not certified by peer review) is the author/funder, who has granted bioRxiv a license to display the preprint in perpetuity. It is made available under aCC-BY-NC-ND 4.0 International license.

277 protection conferred by Ig(M+A)-depleted fraction **(Figure 5B-F)**. BLI analyses revealed loss of
278 virologic control with visible infection at 2-4 dpi and dissemination of virus into the brain at 8 dpi
279 **(Figure 5B, D S5A, B)** with all the mice in the neutrophil-depleted cohort losing weight and
280 succumbing to SARS-CoV-2 challenge, albeit with a delay of 1-3 days **(Figure 5E, F)**. These data
281 correlated with increased viral loads in tissues and enhanced inflammatory cytokine mRNA
282 expression in neutrophil-depleted cohorts prophylactically treated with Ig(M+A)-depleted CCP
283 **(Figure 5G-I, S5C)**. These data suggest a functional interplay between Ig(M+A) and IgG to
284 promote virus neutralization. When Ig(M+A) was depleted, the reliance on Fc-effector
285 mechanisms over direct neutralization by the IgG-harboring fraction was significantly increased
286 for effective virological control and was largely mediated by neutrophils. Thus, when neutralization
287 potency in Ig(M+A) depleted CCP-6 was insufficient to prevent virus infection, IgG-driven Fc-
288 effector recruitment of innate immune cells acted as a second line of defense to promote infected-
289 cell clearance and control virus replication during prophylaxis.
290
291 **Polyclonal IgG and Ig(M+A) Fc-effector Activities Are Required for *In Vivo* CCP Efficacy**
292 **During Therapy**
293 Longitudinal BLI analyses revealed that the *in vivo* efficacy of both IgG and Ig(M+A)-depleted
294 plasma against SARS-CoV-2 was severely compromised compared to undepleted CCP-6 during
295 therapy **(Figure 6A-D)**. SARS-CoV-2-nLuc replicated and disseminated to the brain in 6 out of 7
296 mice in both cohorts that received Ig class-depleted plasma **(Figure 6B-D, G, S6)**. Although 14%
297 of the mice (1 out of 7) in both cohorts survived, body weight and survival analyses showed that
298 mice that received Ig(M+A)-depleted plasma exhibited decelerated body weight loss and delayed
299 mortality (6 dpi vs 8 dpi) compared to those with IgG-depleted plasma **(Figure 6E, F)**. These data
300 suggested that the contribution of IgG was marginally higher than Ig(M+A) to CCP-6 mediated
301 protection. The capacity of CCP-6 to inhibit tissue virus replication and inflammation was also
302 significantly compromised compared to mice treated with undepleted plasma **(Figure 6G-I)**.

bioRxiv preprint doi: https://doi.org/10.1101/2022.06.10.495677; this version posted June 12, 2022. The copyright holder for this preprint (which was not certified by peer review) is the author/funder, who has granted bioRxiv a license to display the preprint in perpetuity. It is made available under aCC-BY-NC-ND 4.0 International license.

Interestingly, cytokine mRNA expression (*CCL2 and CXCL10)* in the lungs of mice that received depleted plasma fractions were significantly higher than the unfractionated CCP-6-treated and the isotype IgG1-treated cohorts (Figure 6I). These data reveal the contribution of both immunoglobulin fractions in dampening exacerbated inflammatory immune responses. Thus, as with prophylaxis, Ig class-depletion analyses suggest a functional interplay between IgG and Ig(M+A) for optimal *in vivo* efficacy of CCP.

VOC Cross-neutralizing Activity in CCPs is Crucial for protection Against VOCs

Recent *in vitro* studies suggest that broad Fc-effector functions elicited by prior infection or vaccination may offer continued protection against emerging variants of concerns (VOCs) despite loss in neutralization (Kaplonek et al., 2022a; Kaplonek et al., 2022b; Richardson et al., 2022). However, if cross-reactive Fc effector functions can provide *in vivo* protective efficacy when neutralization is diminished remains unexplored. We sought to extend these observations to *in vivo* studies using Wuhan-elicited CCPs against heterologous SARS-CoV-2 VOCs B.1.617.2 (Delta) and B.1.352 (Beta). A comparison of neutralizing IC_{50} values using live virus revealed that except for CCP-1 and CCP-5, all other CCPs had comparable neutralizing activities against both WA1 and Delta VOC. In contrast, the ability to neutralize Beta VOC compared to WA1 was significantly diminished for all the CCPs tested **(Figure 7A)**.

We next examined the *in vivo* efficacy of CCPs in K18-hACE2 mice challenged with Delta and Beta VOCs under prophylaxis (-1dpi) and therapy (+2 dpi) **(Figure 7C)**. Prophylaxis using CCP-1 and CCP-2 with low Fc-effector activities failed to protect against both VOCs and the mice exhibited body weight loss and death at 6 dpi like mock-treated control (**Figure 7C, D)**. In contrast, prophylaxis with CCP-4 and CCP-6, that retained considerable Delta VOC-neutralizing activity (IC50 <1/X of plasma) protected mice against Delta and prevented mortality. Prophylaxis with CCP-3 and CCP-5 delayed mortality by 2 and 3 days respectively. Notably, CCP-5, with the weakest neutralizing activity against Delta, delayed mortality which suggested a contribution of

bioRxiv preprint doi: https://doi.org/10.1101/2022.06.10.495677; this version posted June 12, 2022. The copyright holder for this preprint (which was not certified by peer review) is the author/funder, who has granted bioRxiv a license to display the preprint in perpetuity. It is made available under aCC-BY-NC-ND 4.0 International license.

329 Fc- functions towards VOC immunity. These data correlated with lower N mRNA expression in
330 target organs for CCP-4 and 6 followed by CCP-5 and 3-treated mice compared to mock-treated
331 mouse **(Figure 7G, H)**. None of the CCPs analyzed protected against Beta VOC-induced mortality
332 under prophylaxis **(Figure 7D)**. However, treatment with CCP-3, 4, 5 and 6 delayed Beta VOC-
333 induced death by 1-2 days and lowered lung viral loads compared to mock and CCP-1 and 2
334 treated animals **(Figure 7D, H)**. While existing Beta-neutralizing activity likely explained the
335 delayed mortality and reduction in viral loads in CCP-4 and 6 treated mice, Fc-effector functions
336 may have contributed to the marginal protection seen in CCP-3 and 5-treated mice. Notably, none
337 of the CCPs prevented Delta or Beta VOCs-induced mortality under therapy (+2 dpi) **(Figure 7E,**
338 **F)**. We did observe half a day delay in death during Beta VOC infection in mouse under CCP-6
339 therapy. In addition, therapy with CCP-4 and 6 lowered lung viral loads for both Delta and Beta
340 VOC **(Figure 7I, J)**. Thus, while cross-VOC Fc-effector functions contributed to immunity, they
341 were insufficient to prevent VOC-induced mortality in mice and VOC-neutralizing activity in CCPs
342 remained vital for protection against VOCs.
343

344 **Discussion**

345 The constituents of convalescent plasma are complex, and it is difficult to predict their *in*
346 *vivo* efficacies based solely on neutralizing titers or Spike-specific immunoglobulin content. To
347 navigate the intricacies of CCPs, additional measures of selection that track with *in vivo* protection
348 are required and important to guide best practices in future infectious disease outbreaks.
349 Furthermore *in vivo* models that allow testing CPs with protective profiles can help identify suitable
350 properties that can be incorporated in high throughput screening assays *in vitro*. Here we
351 combined the highly susceptible K18-hACE2 mouse model of SARS-CoV-2 with bioluminescence
352 imaging to track virus replication for studying efficacies and characteristics of CCPs that contribute
353 to *in vivo* protection. We show that CCPs with robust Fc effector activities, but low neutralization

bioRxiv preprint doi: https://doi.org/10.1101/2022.06.10.495677; this version posted June 12, 2022. The copyright holder for this preprint (which was not certified by peer review) is the author/funder, who has granted bioRxiv a license to display the preprint in perpetuity. It is made available under aCC-BY-NC-ND 4.0 International license.

354 can protect against homologous SARS-CoV-2 infection under both therapy and prophylaxis.
355 Antibody isotypes, IgG, IgM and IgA collaborated for optimal virologic control and polyclonal Fc-
356 mediated innate immune cell recruitment was required for effective clearing of established SARS-
357 CoV-2 infection. Additionally, despite reduced neutralization, CCPs provided some levels of
358 cross-immunity against Delta and Beta VOCs likely via Fc-mediated effector activities by delaying
359 mortality in mice. Thus, our study underscores the utility of *in vivo* models combined with live
360 tracking of virus replication to identify suitable properties of CCPs with net protective profiles and
361 revealed the contribution of polyclonal Fc-effector functions and antibody classes in combating
362 SARS-CoV-2 and VOCs.

363 We chose CCPs with low neutralizing activities (ID_{50} ≤1:250) together with immune cell
364 depletion to evaluate the *in vivo* efficacy of associated Fc-effector activities. Polyclonal
365 neutralizing activity present in CCP-6 was sufficient to protect mice from SARS-CoV-2-induced
366 mortality during prophylaxis. Despite neutralization playing a major role during CCP-6 prophylaxis,
367 visible infection in the lungs together with transient weight loss upon depletion of innate immune
368 cells revealed a minor yet distinct contribution of Fc-effector functions towards protection. The
369 contribution of Fc- effector mechanism to protection increased significantly when Ig(M+A) was
370 depleted from CCP-6. The combined effect of IgG-driven neutralizing activity and polyclonal Fc-
371 effector functions was however able to compensate for lost Ig(M+A) associated activities to
372 protect mice from SARS-CoV-2. These data also revealed that Ig(M+A) collaborated with IgG to
373 potentiate overall neutralizing activity. A sufficiently potent neutralizing activity alone can counter
374 incoming free virus during SARS-CoV-2 challenge under prophylaxis. However, during therapy,
375 CCPs need to counter both free virus and infected producer cells for curbing virus replication and
376 spread. Thus, in addition to neutralizing activity, for a CCP to be effective therapeutically,
377 polyclonal Fc-mediated innate cell recruitment is likely paramount for clearing pools of infected
378 cells through mechanisms such as ADCC and ADCP. Indeed, we found a critical requirement for

bioRxiv preprint doi: https://doi.org/10.1101/2022.06.10.495677; this version posted June 12, 2022. The copyright holder for this preprint (which was not certified by peer review) is the author/funder, who has granted bioRxiv a license to display the preprint in perpetuity. It is made available under aCC-BY-NC-ND 4.0 International license.

379 neutrophils and macrophages during CCP therapy. Furthermore, both IgG and Ig(M+A) fractions
380 were required during therapy as depleting either, compromised protection. Like prophylaxis, a
381 collaboration between all antibody isotypes was required for effective virologic control during
382 therapy. Exacerbated inflammatory response is one of the hallmarks of SARS-CoV-2-induced
383 disease. In addition to virologic control, we also found that recruitment of innate immune cells
384 through polyclonal Fc-FcR interaction can dampen SARS-CoV-2-induced inflammatory response.
385 Thus CCP-associated polyclonal Fc-effector functions have the potential to mitigate SARS-CoV-
386 2-induced disease newly infected COVID-19 patients.

387 CCP Fc-effector function was rarely measured in COVID-19 clinical studies. Given that
388 the CONCOR-1 trial reported only a loose correlation between neutralizing and Fc-effector
389 functions, one can assume that even studies using stringent CCP selection criteria likely used
390 plasma with variable degrees Fc-effector function (Begin et al., 2021). Developing the capacity to
391 adapt and disseminate Fc-effector function testing rapidly may be key to its wider use in future
392 pandemics and a more optimal use of CCP, directing those with high neutralizing but low Fc-
393 effector function toward prophylaxis trials while reserving those with both high neutralizing and
394 high Fc-effector functions for the acutely ill.

395 The complexities associated with CCP therapy can be resolved using monoclonal
396 antibody cocktails for therapeutic applications (Liu and Shameem, 2022). However, antibody
397 cocktails remain expensive to implement especially in developing nations (Ledford, 2020). They
398 are also subject to neutralization escape by evolving VOCs rendering them ineffective as has
399 been the case with Omicron and its sublineages (Cao et al., 2022; Liu et al., 2022; Planas et al.,
400 2022). In contrast, the ensemble of both nAbs and non-nAbs that CCPs possess make them more
401 resilient to VOCs despite drop in neutralizing titers. Fc-effector mechanisms garnered by SARS-
402 CoV-2-binding antibodies is suggested to remain effective against VOCs (Kaplonek et al., 2022a;
403 Kaplonek et al., 2022b; Richardson et al., 2022) . Whether VOC cross-reactive Fc-effector

bioRxiv preprint doi: https://doi.org/10.1101/2022.06.10.495677; this version posted June 12, 2022. The copyright holder for this preprint (which was not certified by peer review) is the author/funder, who has granted bioRxiv a license to display the preprint in perpetuity. It is made available under aCC-BY-NC-ND 4.0 International license.

activities offer *in vivo* protection remains unexplored. Our *in vivo* efficacy analyses in mice under prophylaxis revealed that Fc-effector activities elicited by the ancestral SARS-CoV-2 that caused the first wave can be effective in delaying death under VOC challenge but were not enough to provide complete protection. These data mirrored our previous analyses where a Fc-enhanced non-nAb did not offer complete protection but delayed mortality in mice (Beaudoin-Bussieres et al., 2022). However, combining Fc-enhanced non-nAb with Fc-compromised nAb completely protected mice when each antibody failed to protect on their own. Thus, cross-reactive Fc-effector functions on their own is likely not enough for protection against VOCs. Polyclonal neutralizing activity, although diminished, form a critical component of the mix with Fc-effector activities to engender protection against VOCs. Overall, our *in vivo* analyses endorse inclusion of Fc-effector activities in addition to neutralization as additional criteria to select CCPs for therapeutic applications. Several high throughput *in vitro* assays exist that can examine multiple signatures of CCPs (Begin et al., 2021; Gunn et al., 2021). *In vivo* efficacy analyses could complement these assays to navigate complex CCP characteristics for identifying those with net protective profiles. Identifying plasma signatures that track with protective or detrimental effects will be key to the success of CP therapy for future infectious disease outbreaks and pandemics.

Supplemental information

6 Supplementary figures

Author contributions

Conceptualization, PDU, AF, RB and PB; Methodology, PDU, IU, MC, AF and RB; Investigation, IU, KS, PDU, GBB, ED, AT, AL; Writing – Original Draft, PDU; Writing – Review & Editing, PDU,

bioRxiv preprint doi: https://doi.org/10.1101/2022.06.10.495677; this version posted June 12, 2022. The copyright holder for this preprint (which was not certified by peer review) is the author/funder, who has granted bioRxiv a license to display the preprint in perpetuity. It is made available under aCC-BY-NC-ND 4.0 International license.

AF, WM, PK, RB, PB, MC, IU; Funding Acquisition, WM, AF, PB, and RB, Resources, WM, PK, AF and RB Supervision, PDU, AF and RB

Acknowledgements

This work was supported by This work was supported by NIH grant R01AI163395 to WM ,le Ministère de l'Économie et de l'Innovation du Québec, Programme de soutien aux organismes de recherche et d'innovation, Foundation du CHUM, CIHR grant nos. 352417 and 177958, a CFI grant, 41027 and a Canada Research Chair on Retroviral Entry no. RCHS0235 950-232424 to AF; Canada's COVID-19 Immunity Task Force (CITF) & Canada Foundation for Innovation (CFI) #41027 to AF, CIHR fellowships to GBB, le Ministère de l'Économie et de l'Innovation du Québec, Fondation du CHU Sainte-Justine Fonds de recherché du Québec – Santé #281662 to PB.

Declaration of Interests

The authors declare no competing interests.

bioRxiv preprint doi: https://doi.org/10.1101/2022.06.10.495677; this version posted June 12, 2022. The copyright holder for this preprint (which was not certified by peer review) is the author/funder, who has granted bioRxiv a license to display the preprint in perpetuity. It is made available under aCC-BY-NC-ND 4.0 International license.

Figure Legends

Figure 1. *In vivo* screening of COVID-19 Convalescent Plasma (CCPs)

(A) A graph depicting WA1-neutralizing activity of indicated CCPs expressed as inhibitory dilution of plasma (ID_{50}) that reduces FFUs by 50% using Vero E6 cells as targets.

(B) %ADCC in the presence of CCP using a 1:1 ratio of parental CEM.NKr cells and CEM.NKr.Spike cells as target cells while PBMCs from uninfected donors were used as effector cells.

(C) A scheme showing experimental design for screening *in vivo* efficacy of indicated CCPs delivered 1ml per 20-25 g body weight of mouse intraperitoneally (i.p.) under prophylaxis (-1dpi) and therapeutically (+2 dpi) in K18-hACE2 mice intranasally (i.n.) challenged with 1 x 10^5 FFU WA1 SARS-CoV-2-nLuc. PBS-treated mice were used as control (Mock).

(D, G) Temporal changes in mouse body weight with initial body weight set to 100% during CCP prophylaxis (-1dpi) and therapy (+2 dpi) for experiment as in C.

(E, H) Fold change in SARS-CoV-2 nucleocapsid (N gene) expression in brain, lung and nose tissues during CCP prophylaxis and therapy for experiment shown in C. The data were normalized to *Gapdh* mRNA expression in the same sample and that in non-infected mice after necropsy.

(F, I) Kaplan-Meier survival curves for evaluating *in vivo* efficacy of CCPs against SARS-CoV-2-nLuc for an experiment as in C.

Figure 2. CCP with Fc-effector Activity Protects K18-hACE2 Mice Against Lethal SARS-CoV-2 Challenge During Prophylaxis and Therapy

(A, G) A scheme showing experimental design for testing *in vivo* efficacy of CCP-2 and CCP-6 (1 ml/ 20-25 g body weight, i.p.) under prophylaxis (-1 dpi) and therapy (+2 dpi) in K18-hACE2 mice intranasally challenged with 1 x 10^5 FFU SARS-CoV-2-nLuc. hIgG1 isotype-treated mice were used as control (Mock).

bioRxiv preprint doi: https://doi.org/10.1101/2022.06.10.495677; this version posted June 12, 2022. The copyright holder for this preprint (which was not certified by peer review) is the author/funder, who has granted bioRxiv a license to display the preprint in perpetuity. It is made available under aCC-BY-NC-ND 4.0 International license.

(B, H) Representative BLI images of SARS-CoV-2-nLuc-infected mice in ventral (v) and dorsal (d) positions for experiment as in A and G. Scale bars denote radiance (photons/sec/cm^2/steradian).

(C, D, I, J) Temporal quantification of nLuc signal as flux (photons/sec) computed non-invasively in indicated tissues.

(E, K) Temporal changes in mouse body weight with initial body weight set to 100% for experiments shown in A and G.

(F, L) Kaplan-Meier survival curves of mice (n = 7 and 4 per group) statistically compared by log-rank (Mantel-Cox) test for experiments as in A and G.

Each curve in C-E and I-K represents an individual mouse. Data in panels C-F and I-L are from two independent experiments and n=2-4 mice per group.

Grouped data in (C-E) and (I-K) were analyzed by 2-way ANOVA followed by Tukey's multiple comparison tests. Statistical significance for group comparisons to mock controls are shown in black, with convalescent plasma CCP-2 are shown in green, and with CCP-6 are shown in cyan. $*$, $p < 0.05$; $**$, $p < 0.01$; $***$, $p < 0.001$; $****$, $p < 0.0001$; Mean values ± SD are depicted. See also Fig S1

Figure 3. Macrophage And Neutrophil Depletion do not Compromise Protection Against SARS-CoV-2 Infection during CCP Prophylaxis in K18-hACE2 Mice

(A) Experimental design to test the contribution of macrophages ($CD45^+Ly6G^-Ly6C^-CD11b^+CD68^+$) and neutrophils $CD45^+CD11b^+Ly6G^+$) in K18-hACE2 mice challenged with SARS-CoV-2-nLuc (1 x 10^5 FFU, i.n.) and treated prophylactically (i.p.; -1 dpi, 1 ml/ 20-25 g body weight) with CCP-6. αCSFR-1 or αLy6G mAbs (i.p., 20 mg/kg body weight) were used to deplete macrophages and neutrophils respectively every 48h starting two days before infection. Human and rat isotype mAb-treated cohorts served as controls (Iso). Animals were followed by non-invasive BLI every 2 days as indicated.

bioRxiv preprint doi: https://doi.org/10.1101/2022.06.10.495677; this version posted June 12, 2022. The copyright holder for this preprint (which was not certified by peer review) is the author/funder, who has granted bioRxiv a license to display the preprint in perpetuity. It is made available under aCC-BY-NC-ND 4.0 International license.

493 (B) Representative BLI images of SARS-CoV-2-nLuc-infected mice in ventral (v) and dorsal (d)
494 positions. Scale bars denote radiance (photons/sec/cm^2/steradian).
495 (C-D) Temporal quantification of nLuc signal as flux (photons/sec) computed non-invasively.
496 (E) Temporal changes in mouse body weight with initial body weight set to 100% for an
497 experiment shown in A.
498 (F) Kaplan-Meier survival curves of mice (n = 4 per group) statistically compared by log-rank
499 (Mantel-Cox) test for experiment as in A.
500 (G, H) *Ex vivo* imaging of indicated organs and quantification of nLuc signal as flux(photons/sec)
501 after necropsy.
502 (I) Fold change in SARS-CoV-2 nucleocapsid (N gene) expression in brain, lung and nose tissues.
503 The data were normalized to *Gapdh* mRNA expression in the same sample and that in non-
504 infected mice after necropsy.
505 (J) Viral loads (nLuc activity/mg) in indicated tissue measured on Vero E6 cells as targets.
506 Undetectable virus amounts were set to 1.
507 (K, L) Fold change in cytokine mRNA expression in brain and lung tissues. The data were
508 normalized to *Gapdh* mRNA expression in the same sample and that in non-infected mice after
509 necropsy.
510 Viral loads (I, J) and inflammatory cytokine profile (K, L) were determined after necropsy for mice
511 that succumb to infection at 6 dpi and for surviving mice at 10 dpi. Each curve in C-E and each
512 data point in H-L represents an individual mouse. Data in panels C-L are from two independent
513 experiments and n=2 mouse per group.
514 Grouped data in (C-E), (H-L) were analyzed by 2-way ANOVA followed by Tukey's multiple
515 comparison tests. Statistical significance for group comparisons to isotype control are shown in
516 black, with CCP-6 are shown in cyan, with CCP-6+αCSF1R are shown in green and with CCP-6
517 αLy6G are shown in red. ∗, $p < 0.05$; ∗∗, $p < 0.01$; ∗∗∗, $p < 0.001$; ∗∗∗∗, $p < 0.0001$; Mean values
518 ± SD are depicted. See also Figure S2

bioRxiv preprint doi: https://doi.org/10.1101/2022.06.10.495677; this version posted June 12, 2022. The copyright holder for this preprint (which was not certified by peer review) is the author/funder, who has granted bioRxiv a license to display the preprint in perpetuity. It is made available under aCC-BY-NC-ND 4.0 International license.

Figure 4. Macrophages and Neutrophils Are Required to Eliminate Established SARS-CoV-2 Infection During CCP Therapy in K18-hACE2 Mice

(A) Experimental design to test the contribution of macrophages ($CD45^+CD11b^+CD68^+$) and neutrophils ($CD45^+CD11b^+Ly6G^+$) in K18-hACE2 mice therapeutically treated at 2 dpi with CCP-6 (i.p., 1 ml/ 20-25 g body weight) after challenge with SARS-CoV-2-nLuc (i.n., 1 x 10^5 FFU). αCSF1R or αLy6G mAbs (i.p., 20 mg/kg body weight) were used to deplete macrophages and neutrophils respectively every 48h starting at 0 dpi. Human and/or rat isotype mAb treated cohorts served as controls (Isotype). The mice were followed by non-invasive BLI every 2 days from the start of infection.

(B) Representative BLI images of SARS-CoV-2-nLuc-infected mice in ventral (v) and dorsal (d) positions. Scale bars denote radiance (photons/sec/cm^2/steradian).

(C-D) Temporal quantification of nLuc signal as flux (photons/sec) computed non-invasively.

(E) Temporal changes in mouse body weight with initial body weight set to 100% for an experiment shown in A.

(F) Kaplan-Meier survival curves of mice (n = 4 per group) statistically compared by log-rank (Mantel-Cox) test for experiment as in A.

(G) Viral loads (nLuc activity/mg) from indicated tissue using Vero E6 cells as targets. Undetectable virus amounts were set to 1.

(H, I) Fold change in cytokine mRNA expression in brain and lung tissues. The data were normalized to *Gapdh* mRNA expression in the same sample and that in non-infected mice after necropsy.

Viral loads (G) and inflammatory cytokine profile (H, I) were determined at 6 dpi for mice that succumbed to infection and for surviving mice at 10 dpi after necropsy. Each curve in (C-E) and each data point in (G-I) represents an individual mouse. Data in panels C-I are from two independent experiments and n=2-3 mice per group.

bioRxiv preprint doi: https://doi.org/10.1101/2022.06.10.495677; this version posted June 12, 2022. The copyright holder for this preprint (which was not certified by peer review) is the author/funder, who has granted bioRxiv a license to display the preprint in perpetuity. It is made available under aCC-BY-NC-ND 4.0 International license.

Grouped data in (C-E), (G-I) were analyzed by 2-way ANOVA followed by Tukey's multiple comparison tests. Statistical significance for group comparisons to isotype control are shown in black, with CCP-6-treated cohorts are shown as cyan, CCP-6-treated neutrophil-depleted cohorts are shown in red, and with CCP-treated macrophage-depleted cohorts are shown in green. $*$, $p < 0.05$; $**$, $p < 0.01$; $***$, $p < 0.001$; $****$, $p < 0.0001$; Mean values ± SD are depicted. See also Figure S3.

Figure 5. Polyclonal IgGs in CCP Predominantly Contribute to Protection During Prophylaxis in SARS-CoV-2-infected K18-hACE2 Mice.

(A) Experimental design to test *in vivo* efficacies of IgG- and Ig(M+A)-depleted CCP-6 (1 ml x 2 i.p. injections, 3 h apart) in SARS-CoV-2-nLuc infected K18-hACE2 mice (i.n., 1 $x10^5$ FFU) under prophylaxis (-1 dpi). For CCP-6 treatment, plasma was diluted to equalize IgG content of Ig(M+A)-depleted plasma. αLy6G mAb (i.p., 20 mg/kg body weight) was used to deplete neutrophils respectively every 48h starting two days before infection. Mice treated with hIgG1 served as controls (Iso). The mice were followed by non-invasive BLI every 2 days from the start of infection.

(B) Representative BLI images of SARS-CoV-2-nLuc-infected mice in ventral (v) and dorsal (d) positions. Scale bars denote radiance (photons/sec/cm^2/steradian).

(C-D) Temporal quantification of nLuc signal as flux (photons/sec) computed non-invasively.

(E) Temporal changes in mouse body weight with initial body weight set to 100% for an experiment shown in A.

(F) Kaplan-Meier survival curves of mice (n = 4 per group) statistically compared by log-rank (Mantel-Cox) test for experiment as in A.

(G) Viral loads (nLuc activity/mg) from indicated tissues using Vero E6 cells as targets. Undetectable virus amounts were set to 1.

bioRxiv preprint doi: https://doi.org/10.1101/2022.06.10.495677; this version posted June 12, 2022. The copyright holder for this preprint (which was not certified by peer review) is the author/funder, who has granted bioRxiv a license to display the preprint in perpetuity. It is made available under aCC-BY-NC-ND 4.0 International license.

(H, I) Fold change in cytokine mRNA expression in brain and lung tissues. The data were normalized to *Gapdh* mRNA expression in the same sample and that in non-infected mice after necropsy.

Viral loads (G) and inflammatory cytokine profile (H, I) were determined at the time of death at 6 dpi or 10 dpi for surviving mice after necropsy. Each curve in C-E and each data point in G-I represents an individual mouse. Data in panels C-I are from are from two independent experiments and n=2 mice per group Grouped data in (C-E), (G-I) were analyzed by 2-way ANOVA followed by Tukey's multiple comparison tests. Statistical significance for group comparisons to isotype control are shown in black, with IgG equalized CCP-6 are shown in cyan, with IgG-depleted CCP-6 are shown in red, with Ig(M+A)-depleted CCP-6 are shown in green and with Ig(M+A)-depleted CCP under neutrophil depletion are shown in orange. $*$, $p < 0.05$; $**$, $p < 0.01$; $***$, $p < 0.001$; $****$, $p < 0.0001$; Mean values ± SD are depicted. See also Figure S4.

Figure 6. Antibody Classes Collaborate to Achieve Maximal *In Vivo* Protection during CCP Therapy in SARS-CoV-2-infected K18-hACE2 Mice

(A) Experimental design to test *in vivo* efficacies of IgG- and Ig(M+A)-depleted CCP-6 (1 ml x 2 i.p. injections, 1 h apart) in SARS-CoV-2-nLuc infected mice K18-hACE2 mice (i.n., 1 x10^5 FFU) under therapy (+2 dpi). For CCP-6 treatment, plasma was diluted to equalize IgG content of Ig(M+A)-depleted plasma. Mice treated with hIgG1 served as controls (Iso). The mice were followed by non-invasive BLI every 2 days from the start of infection.

(B) Representative BLI images of SARS-CoV-2-nLuc-infected mice in ventral (v) and dorsal (d) positions. Scale bars denote radiance (photons/sec/cm^2/steradian).

(C-D) Temporal quantification of nLuc signal as flux (photons/sec) computed non-invasively.

(E) Temporal changes in mouse body weight with initial body weight set to 100% for an experiment shown in A.

bioRxiv preprint doi: https://doi.org/10.1101/2022.06.10.495677; this version posted June 12, 2022. The copyright holder for this preprint (which was not certified by peer review) is the author/funder, who has granted bioRxiv a license to display the preprint in perpetuity. It is made available under aCC-BY-NC-ND 4.0 International license.

(F) Kaplan-Meier survival curves of mice (n = 7 per group) statistically compared by log-rank (Mantel-Cox) test for experiment as in A.

(G) Viral loads (FFUs/mg) from indicated tissue using Vero E6 cells as targets. Undetectable virus amounts were set to 1.

(H, I) Fold change in cytokine mRNA expression in brain and lung tissues. The data were normalized to *Gapdh* mRNA expression in the same sample and that in non-infected mice after necropsy.

Viral loads (G) and inflammatory cytokine profile (H, I) were determined at the time of death for mice that succumbed to infection (F) and at 18 dpi for surviving mice Each curve in C-E and each data point in G-I represents an individual mouse. Data in panels C-I are from from two to three independent experiments n=2-3 mouse per group.

Grouped data in (C-E), (G-I) were analyzed by 2-way ANOVA followed by Tukey's multiple comparison tests. Statistical significance for group comparisons to isotype control are shown in black, with IgG-equated CCP-6 are shown in cyan, with IgG-depleted CCP-6 are shown in red and with Ig(M+A)-depleted CCP-6 are shown in green. ∗, $p < 0.05$; ∗∗, $p < 0.01$; ∗∗∗, $p < 0.001$; ∗∗∗∗, $p < 0.0001$; Mean values ± SD are depicted. See also Figure S6.

Figure 7. Fc-mediated cross-protective efficacy profiles of WA1-elicited CCPs against Delta and Beta VOCs in K18-hACE2 mice.

(A) A graph depicting WA1, Delta and Beta-neutralizing activity of indicated CCPs expressed as inhibitory concentration of plasma (IC_{50}) that reduces FFUs by 50% using Vero E6 cells as targets. One-way Anova with Dunnett's multiple comparisons test was used to determine is if Delta and Beta VOC neutralizing titers in CCPs differed significantly to WA1-neutralizing titers. $p < 0.05$; ∗∗, $p < 0.01$; ∗∗∗, $p < 0.001$; ∗∗∗∗, $p < 0.0001$; Mean values ± SD are depicted.

(B) A scheme showing experimental design for screening *in vivo* efficacy of indicated CCPs delivered 1ml per 20-25 g body weight of mouse intraperitoneally (i.p.) under prophylaxis (-1dpi)

bioRxiv preprint doi: https://doi.org/10.1101/2022.06.10.495677; this version posted June 12, 2022. The copyright holder for this preprint (which was not certified by peer review) is the author/funder, who has granted bioRxiv a license to display the preprint in perpetuity. It is made available under aCC-BY-NC-ND 4.0 International license.

and therapeutically (+2 dpi) in K18-hACE2 mice intranasally (i.n.) challenged with 1 x 10^5 FFU of B.1.617.2 (Delta VOC) or B.1.351 (Beta VOC). PBS-treated mice were used as control (Mock).

(C-F) Temporal changes in mouse body weight with initial body weight set to 100% during CCP prophylaxis (-1dpi) and therapy (+2 dpi) for experiment as in C in mice challenged with Delta and Beta VOC.

(G-J) Fold change in SARS-CoV-2 nucleocapsid (N gene) expression in brain, lung and nose tissues during CCP prophylaxis and therapy for experiment shown in C. The data were normalized to *Gapdh* mRNA expression in the same sample and that in non-infected mice after necropsy.

bioRxiv preprint doi: https://doi.org/10.1101/2022.06.10.495677; this version posted June 12, 2022. The copyright holder for this preprint (which was not certified by peer review) is the author/funder, who has granted bioRxiv a license to display the preprint in perpetuity. It is made available under aCC-BY-NC-ND 4.0 International license.

STAR Methods

KEY RESOURCES TABLE

REAGENT or RESOURCE	SOURCE	IDENTIFIER
Antibodies		
Fc block anti mouse-CD16/CD32 (93)	BioLegend Inc	Cat # 101302 RRID: AB_312801
PE anti-mouse CD11b (M1/70)	BioLegend Inc	Cat # 101207 RRID: AB_312790
APC/Cy7 anti-mouse Ly-6C (HK1.4)	BioLegend Inc	Cat #128025 RRID: AB_10643867
APC/Cy7 anti-mouse Ly-6G (Clone 1A8)	BioLegend Inc	Cat #127617 RRID:AB_1877262
Alexa Fluor® 488 anti-mouse Ly-6G (Clone 1A8)	BioLegend Inc	Cat # 127626 RRID: AB_2561340
APC Rat anti-mouse CD45 (30-F11)	BD-Pharmingen	Cat # 559864 RRID:AB_398672
Alexa Fluor® 488 anti-mouse CD45 (Clone 30-F11)	BioLegend Inc	Cat # 103122 RRID: AB_493531
InVivoMAb anti-mouse LY6G (clone: 1A8) for neutrophil depletion	Bio X Cell	Cat # BE0075-1 RRID: AB_1107721
InVivoMAb anti-mouse CSF1R (CD115) for macrophage depletion	Bio X Cell	Cat # BE0213 RRID: AB_ 2687699
InVivoMab rat IgG2a clone C1.18.4; Isotype controls for macrophage and neutrophil depletion	Bio X Cell	Cat # BE0085 RRID: AB_1107771
InVivoMAb human IgG1 isotype control	Bio X Cell	Cat # BE0297 RRID: AB_2687817
Goat anti-Human IgG (H+L) Cross-Adsorbed Secondary Antibody, Alexa Fluor 647	Invitrogen	Cat # A-21445; RRID: AB_2535862
Goat anti-Mouse IgG (H+L) Cross-Adsorbed Secondary Antibody, Alexa Fluor 647	Invitrogen	Cat # A-21235; RRID: AB_2535804
Goat anti-Human IgG Fc Cross-Adsorbed Secondary Antibody, HRP	Invitrogen	Cat # A18823; RRID: AB_2535600
Goat Anti-human IgM (μ-chain specific) 1 mg	Sigma-Aldrich	I01759-1MG

bioRxiv preprint doi: https://doi.org/10.1101/2022.06.10.495677; this version posted June 12, 2022. The copyright holder for this preprint (which was not certified by peer review) is the author/funder, who has granted bioRxiv a license to display the preprint in perpetuity. It is made available under aCC-BY-NC-ND 4.0 International license.

Goat anti-human IgA α chain spécific	Jackson ImmunoResearch		109-005-011	
Human IgA subclasses standard serum	Cedarlane		NOR-04	
Peroxidase AffiniPure F(ab')$_2$ Fragment Goat Anti-Human Serum IgA, α chain specific	Jackson ImmunoResearch		109-036-011	
Goat anti-Human IgG Fc specific	Jackson ImmunoResearch		109-005-098	
Serum Human Standard à 9,5 mg/mL	Cedarlane		NOR-01	
Peroxidase AffiniPure Goat Anti-Human IgG (H+L) (min X Bov, Hrs, Ms Sr Prot)	Jackson ImmunoResearch		109-035-088	
Goat anti-human IgM Fc specific	Jackson ImmunoResearch		109-005-129	
Low control human serum	Cedarlane		35-S4321H000-L4	
Peroxidase AffiniPure Goat Anti-Human IgA + IgG + IgM (H+L)	Jackson ImmunoResearch		109-035-064	
IgM from human serum	Sigma Aldrich		I-8260	
Deposited data				
Bacterial and Virus Strains				
SARS-CoV-2-nLuc (strain 2019-nCoV/USA_WA1/2020)	Craig B Wilen (Yale University)		K. Plante and Pei-Yong Shi, World Reference Center for Emerging Viruses and Arboviruses, University of Texas Medical Branch)	
SARS-CoV-2 USA-WA1/2020	BEI resources		Cat # NR-52281	
SARS-CoV-2, Isolate hCoV-19/USA/PHC658/2021 (Delta Variant)	BEI resources		Cat # NR-55611	
SARS-CoV-2, Isolate hCoV-19/USA/MD-HP01542/2021	BEI resources		Cat # NR-55282	
Biological Samples	Age	M/F	Days post infection at collection	ABO (Rh)
CCP-1	50	M	50	AB (+)
CCP-2	58	M	78	A (+)
CCP-3	49	M	77	O (+)
CCP-4	23	F	unknown	O (+)
CCP-5	30	M	30	O (-)
CCP-6	51	M	69	A (+)
Primary human peripheral blood mononuclear cells (PBMCs)	FRQS AIDS network		N/A	

bioRxiv preprint doi: https://doi.org/10.1101/2022.06.10.495677; this version posted June 12, 2022. The copyright holder for this preprint (which was not certified by peer review) is the author/funder, who has granted bioRxiv a license to display the preprint in perpetuity. It is made available under aCC-BY-NC-ND 4.0 International license.

Chemicals, Peptides, and Recombinant Proteins		
Liberase TL Research Grade	Sigma-Aldrich	Cat# 5401020001
Dispase (5U/ml)	STEMCELL technologies	Catalog # 07913
DNAse I recombinant, RNAse-free	Roche	Ref # 04716728001
Gibco™ RPMI 1640 medium	Thermo Fisher Scientific	Cat # 11875093
Gibco™ Dulbecco's modified Eagle's medium (DMEM)	Thermo Fisher Scientific	Cat # 11965118
Gibco™ MEM Non-essential amino acid (NEAA) solution	Thermo Fisher Scientific	Cat # 11140050
Gibco™ Penicillin-streptomycin solution (10,000 U/ml)	Thermo Fisher Scientific	Cat # 15140122
Gibco™ Dulbecco's Phosphate Buffered Saline (DPBS)	Thermo Fisher Scientific	Cat # 14190144
Gibco™ L-Glutamine (200mM)	Thermo Fisher Scientific	Cat # 25030081
Gibco™ 0.05% Trypsin-EDTA, phenol red	Thermo Fisher Scientific	Cat # 25300054
Fetal bovine serum	Atlanta Biologicals	Cat # S11550
eBioscience™ RBC Lysis Buffer (1X)	invitrogen	Cat # 00-4333-57
Bovine Serum Albumin (BSA)	Sigma-Aldrich	Cat# A9647-100G CAS: 9048-46-8
Accutase	BioLegend Inc	Cat # 423201
0.05% Trypsin-EDTA (1X)	Life Technologies	Cat # 25300-054
K3 EDTA 15% Solution	Fisher Scientific	Cat # BD 366450
Sodium pyruvate (100 mM)	Life technologies	Ref # 11360-070
2-Mercaptoethanol	Sigma-Aldrich	Cat # M3148
L-Glutamine (200mM)	Life technologies	Ref # 25030-081
Tris-buffered saline (TBS)	Thermo Fisher Scientific	Cat # BP24711
BD Cytofix/Cytoperm™	BD Biosciences	Cat # 554722
BD Perm/Wash™	BD Biosciences	Cat # 554723
Passive lysis buffer	Promega	Cat # E1941
Paraformaldehyde (16% PFA)	Electron Microscopy Sciences	Cat # 19200 CAS: 30525-89-4

bioRxiv preprint doi: https://doi.org/10.1101/2022.06.10.495677; this version posted June 12, 2022. The copyright holder for this preprint (which was not certified by peer review) is the author/funder, who has granted bioRxiv a license to display the preprint in perpetuity. It is made available under aCC-BY-NC-ND 4.0 International license.

Rat serum	Stemcell Biotechnologies	Cat # 13551
Dimethyl sulfoxide (DMSO)	Sigma-Aldrich	Cat # D2650-5X5ML CAS: 67-68-5
Sodium azide	Sigma-Aldrich	Cat # S-8032 EC No: 247-852-1
Glycine	American Bioanalytical	Cat # AB00730-01000 CAS: 56-40-6
The PEG-it Virus precipitation solution (5X)	System Bioscience	Cat # LV810A-1
Avicel® Pharma Grade	FMC	Cat # RC-581 NF 10.20944/preprints202005.0264.v1
Puromycin dihydrochloride	Millipore Sigma	Cat # P8833
D-Luciferin potassium salt	Thermo Fisher Scientific	Cat # L2916
LIVE/DEAD Fixable AquaVivid Cell Stain	Thermo Fisher Scientific	Cat # L34957
Cell proliferation dye eFluor670	Thermo Fisher Scientific	Cat # 65-0840-85
Cell proliferation dye eFluor450	Thermo Fisher Scientific	Cat # 65-0842-85
SARS-CoV-2 S2 ectodomain C-His tag protein	BEI Resources	NR-53799
SIGMAFAST OPD	EMD Millipore	Cat # P9187
Ethanolamine	Sigma Aldrich	E0135-100ml
Sodium chloride 5M	Sigma Aldrich	59222C-500mL
Hydrochloric acid	Biolab	351285-212
Sodium acetate	Sigma Aldrich	S2889-250g
Carbonate, 0.5M buffer soln., pH 9.6 250mL	Fisher Scientific	AAJ62610AK
NHS Act Sepharose® 4 Fast Flow	Sigma Aldrich	GE17-0906-01
Peptide M/Agarose 2 mL	Cedarlane	GEL-PDM-2
Sodium bicarbonate	Sigma Aldrich	S6014
Sodium carbonate	Sigma Aldrich	S2127
Tween-20	Fisher Scientific	BP337-500
Casein, Hammarsten bovine	Sigma Aldrich	E0789-500g
TMB soluble reagent high sensitivity	ESBE Scientific	SCY-TM4999
H_2SO_4 10N	Fisher Scientifc	SA200-1
Critical Commercial Assays		

bioRxiv preprint doi: https://doi.org/10.1101/2022.06.10.495677; this version posted June 12, 2022. The copyright holder for this preprint (which was not certified by peer review) is the author/funder, who has granted bioRxiv a license to display the preprint in perpetuity. It is made available under aCC-BY-NC-ND 4.0 International license.

Nano-Glo Luciferase Assay System (nanoluc substrate)	Promega	Cat # N1120
Pierce™ Gaussia Luciferase Glow Assay Kit	ThermoFisher Scientific	Cat # 16160
KAPA SYBR FAST qPCR Master Mix (2X) Kit	KAPA Biosystems	Cat # KK4600 and KK4601
Ambion DNase I (RNase-free)	ThermoFisher Scientific	Cat # AM2222
RNeasy Mini Kit (50)	Qiagen	Cat #/ID 74104
iScript advanced cDNA kit	Bio Rad	Cat #1725038
iQ Multiplex Powermix	Bio Rad	Cat # 1725848
iScript™ cDNA Synthesis Kit	Bio Rad	Cat # 95047-100
Protein G HP SpinTrap	Cytiva	28903134
Experimental Models: Cell Lines		
Vero E6 (female, Chlorocebus sabaeus)	ATCC	Cat # CRL-1586; RRID: CVCL_0574
Vero E6-TMPRSS2 (female, Chlorocebus sabaeus)	Craig B. Wilen, Yale University	N/A
HEK293 (female, Homo sapiens)	ATCC	Cat # CRL-1573; RRID: CVCL_0045
HEK293T (female, Homo sapiens)	ATCC	Cat # CRL-3216; RRID: CVCL_0063
293T-ACE2 (female, Homo sapiens)	(Prevost et al., 2020)	N/A
Cf2Th (female, Canis lupus familiaris)	ATCC	Cat # CRL-1430; RRID: CVCL_3363
CEM.NKr-CCR5+ (female, Homo sapiens)	NIH AIDS Reagent Program	Cat # 4376; RRID: CVCL_X623
CEM.NKr-Spike (female, Homo sapiens)	(Anand et al., 2021a)	N/A
TZM-bl (female, Homo sapiens)	NIH AIDS Reagent Program	Cat # 8129; RRID: CVCL_B478
THP-1 (male, Homo sapiens)	ATCC	Cat # TIB-202; RRID: CVCL_0006
Experimental Models: Organisms/Strains		
C57BL/6J (B6) (males and females); 6-12 weeks old	The Jackson Laboratory	The Jackson Laboratory Stock No: 000664 RRID: IMSR_JAX:000664
B6.Cg-Tg(K18-ACE2)2Prlmn/J (males and females); 6-12 weeks old	The Jackson Laboratory	Stock No: 034860 RRID:IMSR_JAX:034860
Oligonucleotides		

bioRxiv preprint doi: https://doi.org/10.1101/2022.06.10.495677; this version posted June 12, 2022. The copyright holder for this preprint (which was not certified by peer review) is the author/funder, who has granted bioRxiv a license to display the preprint in perpetuity. It is made available under aCC-BY-NC-ND 4.0 International license.

SARS-CoV-2 N F: 5'-ATGCTGCAATCGTGCTACAA-3'	Yale School of Medicine, W. M. Keck Foundation, Oligo Synthesis Resource	N/A
SARS-CoV-2 N R: 5'-GACTGCCGCCTCTGCTC-3'	Yale School of Medicine, W. M. Keck Foundation, Oligo Synthesis Resource	N/A
FAM-Gapdh	Bio Rad	Cat # 12001950
HEX-IL6	Bio Rad	Cat # 10031228
TEX615-CCL2	Bio Rad	Cat # 10031234
Cy5-CXCL10	Bio Rad	Cat # 10031231
Cy5.5-IFNg	Bio Rad	Cat # 10031237
Transgene Forward: GAC CCC TGA GGG TTT CAT ATA G	Yale School of Medicine, W. M. Keck Foundation, Oligo Synthesis Resource	#53437, Genotyping primers for K18-hACE2 mice. The Jackson Laboratory
Common: CAC CAA CAC AGT TTC CCA AC	Yale School of Medicine, W. M. Keck Foundation, Oligo Synthesis Resource	#53438, Genotyping primers for K18-hACE2 mice. The Jackson Laboratory
Wildtype forward: AAG TTG GAG AAG ATG CTG AAA GA	Yale School of Medicine, W. M. Keck Foundation, Oligo Synthesis Resource	#53439, Genotyping primers for K18-hACE2 mice. The Jackson Laboratory
Recombinant DNA		
pNL4.3 R-E- Luc	NIH AIDS Reagent Program	Cat # 3418
pSVCMV-IN-VSV-G	Lodge et al.	N/A
Lentiviral packaging plasmids (pLP1, pLP2)	(Liu et al., 2013)	N/A
pLenti-C-mGFP-P2A-Puro-ACE2	OriGene	Cat # RC208442L4
pIRES2-eGFP vector	Clontech	Cat # 6029-1
pLTR-Tat	(Finzi et al., 2010)	N/A
Software and Algorithms		
Accuri CSampler software	BD Biosciences	
FlowJo v10	Treestar	https://www.flowjo.com/ RRID:SCR_008520
Nikon-Elements AR Analysis v4.13 and Acquisition v4.5	Nikon	RRID:SCR_014329
Adobe Photoshop CC	Adobe Systems Inc	RRID:SCR_014199
Adobe Illustrator CC	Adobe Systems Inc	RRID:SCR_010279
BioRender (schematics in figures)	BioRender.com	RRID:SCR_018361

bioRxiv preprint doi: https://doi.org/10.1101/2022.06.10.495677; this version posted June 12, 2022. The copyright holder for this preprint (which was not certified by peer review) is the author/funder, who has granted bioRxiv a license to display the preprint in perpetuity. It is made available under aCC-BY-NC-ND 4.0 International license.

CFX MaestroTM Software (qPCR analyses)	Bio-rad Inc	RRID:SCR_018064
Graphpad Prism v9.0.1	GraphPad Software	https://www.graphpad.com/ RRID:SCR_002798
Living Image software	Perkin Elmer	http://www.perkinelmer.com/catalog/category/id/living%20image%20software RRID:SCR_014247
Gen5 microplate reader and imager software	Biotek	RRID:SCR_017317
Other		
TriStar LB 941 Multimode Microplate Reader and Luminometer	BERTHOLD TECHNOLOGIES GmbH & Co. KG	Mothes and Finzi Lab
BD Biosciences C6 Accuri Flow Cytometer,	BD Biosciences	Yale, MMPATH, Central Facility RRID:SCR_019591
BD LSR II Flow Cytometer	BD Biosciences	https://medicine.yale.edu/immuno/flowcore/
C1000 Touch thermal cycler	Bio-Rad	RRID:SCR_019688
CFX Connect™ Real-Time PCR Detection System	Bio-Rad	RRID:SCR_018064
Nanodrop Spectrophotometer ND-1000	ThermoFisher Scientific	RRID:SCR_016517
27G × ½" insulin syringe with needle	TERUMO	Cat # SS*05M2713
31G insulin syringe	BD Biosciences	Cat # 328468
70 µm Nylon cell strainer	FALCON	Cat # 352350
Acrodisc 25 mm Syringe Filter w/0.45 µm HT Tuffryn Membrane	PALL Life Sciences	Cat # 4184
96-well white plates for luciferase assays	Costar	Cat # 3917
Cryotubes	Thermo Scientific Nunc	Cat # 340711
Polystyrene Round-bottom Tube	FALCON	Ref # 352058
Optical Flat 8-Cap Strips for 0.2 ml tube stripes/plates	Bio-Rad	Cat # TCS0803
Individual PCR tubes 8-tube Strip, clear	Bio-Rad	Cat # TLS0801
ThermalGrid Rigid Strip PCR tubes	Denville Scientific INC	Ref # C18064
96 well U bottom plate	FALCON	Ref # 353077
XIC-3 animal isolation chamber	PerkinElmer	N/A
Perkin Elmer IVIS Spectrum In-Vivo Imaging System	PerkinElmer	Yale University ABSL-3 facility. RRID:SCR_018621
RAS-4 Rodent Anesthesia System	PerkinElmer	CLS146737

bioRxiv preprint doi: https://doi.org/10.1101/2022.06.10.495677; this version posted June 12, 2022. The copyright holder for this preprint (which was not certified by peer review) is the author/funder, who has granted bioRxiv a license to display the preprint in perpetuity. It is made available under aCC-BY-NC-ND 4.0 International license.

Synergy LX multi-mode reader	Biotek	RRID:SCR_019763
Millex-GV Filter, 0.22uM	Fisher Scientific	SLGV013SL
MicroSpin Columns, 50 Pieces	Cytiva	27356501
Immulon 2HB 96-Wells Flat bottom	VWR	62402-972
EBA 21 centrifuge	Hettich	1004-31
Legend 21R Micro centrifuge	Thermo Scientific	75002446
Micro plate reader Synergy	Biotek	H1
Microplate washer 405 TS	Biotek	405TSRSQ

RESOURCE AVAILABILITY

Lead Contact: Pradeep Uchil (Pradeep.uchil@yale.edu

Requests for resources and reagents should be directed to and will be fulfilled by the Lead Contact, Pradeep Uchil (pradeep.uchil@yale.edu),

Materials Availability

All other unique reagents generated in this study are available from the corresponding authors with a completed Materials Transfer Agreement.

Data and Code Availability

All the data that support the findings of this study are available from the corresponding authors upon reasonable request.

EXPERIMENTAL MODEL AND SUBJECT DETAILS

Cell and Viruses

Vero E6 (CRL-1586, American Type Culture Collection (ATCC), were cultured at 37°C in RPMI supplemented with 10% fetal bovine serum (FBS), 10 mM HEPES pH 7.3, 1 mM sodium pyruvate, 1× non-essential amino acids, and 100 U/ml of penicillin–streptomycin. The 2019n-CoV/USA_WA1/2019 isolate of SARS-CoV-2 expressing Nanoluc luciferase was obtained from Craig B Wilen, Yale University and generously provided by K. Plante and Pei-Yong Shi, World Reference Center for Emerging Viruses and Arboviruses, University of Texas Medical Branch) (Xie et al., 2020). SARS-CoV-2 USA-WA1/2020, B.1.617.2 (Delta) and B.1.351 (Beta) isolates without reporters was obtained through BEI Resources. Viruses were propagated in Vero E6

bioRxiv preprint doi: https://doi.org/10.1101/2022.06.10.495677; this version posted June 12, 2022. The copyright holder for this preprint (which was not certified by peer review) is the author/funder, who has granted bioRxiv a license to display the preprint in perpetuity. It is made available under aCC-BY-NC-ND 4.0 International license.

TMPRSS2 by infecting them in T150 cm^2 flasks at a MOI of 0.1. The culture supernatants were collected after 72 h when cytopathic effects were clearly visible. The cell debris was removed by centrifugation and filtered through 0.45-micron filter to generate virus stocks. Viruses were concentrated by adding one volume of cold (4 °C) 4x PEG-it Virus Precipitation Solution (40 % (w/v) PEG-8000 and 1.2 M NaCl; System Biosciences) to three volumes of virus-containing supernatant. The solution was mixed by inverting the tubes several times and then incubated at 4°C overnight. The precipitated virus was harvested by centrifugation at 1,500 × g for 60 minutes at 4°C. The concentrated virus was then resuspended in PBS then aliquoted for storage at −80°C. All work with infectious SARS-CoV-2 was performed in Institutional Biosafety Committee approved BSL3 and A-BSL3 facilities at Yale University School of Medicine using appropriate positive pressure air respirators and protective equipment. CEM.NKr, CEM.NKr-Spike, and peripheral blood mononuclear cells (PBMCs) were maintained at 37°C under 5% CO_2 in RPMI media, supplemented with 10% FBS and 100 U/mL penicillin/ streptomycin. 293T (or HEK293T), 293T-ACE2 (Prevost et al., 2020) cells were maintained at 37°C under 5% CO_2 in DMEM media, supplemented with 5 % FBS and 100 U/mL penicillin/ streptomycin. CEM.NKr (NIH AIDS Reagent Program) is a T lymphocytic cell line resistant to NK cell-mediated lysis. CEM.NKr-Spike stably expressing SARS-CoV-2 Spike were used as target cells in ADCC assays (Anand et al., 2021; Beaudoin-Bussieres et al., 2021). PBMCs were obtained from healthy donor through leukapheresis and were used as effector cells in ADCC assay.

Ethics statement

CCP was obtained from individuals who were infected during the first wave of the pandemic, after at least fourteen days of resolution of COVID-19 symptoms (Perreault et al., 2020). All participants consented to the study (CER #2020-004). PBMCs from healthy individuals as a source of effector cells in our ADCC assay were obtained under CRCHUM institutional review board (protocol #19.381). Research adhered to the standards indicated by the Declaration of Helsinki. All

bioRxiv preprint doi: https://doi.org/10.1101/2022.06.10.495677; this version posted June 12, 2022. The copyright holder for this preprint (which was not certified by peer review) is the author/funder, who has granted bioRxiv a license to display the preprint in perpetuity. It is made available under aCC-BY-NC-ND 4.0 International license.

677 participants were adults and provided informed written consent prior to enrollment in accordance
678 with Institutional Review Board approval.

679 **Plasma samples**

680 Recovered COVID-19 patients who have received a COVID-19 diagnosis by the Québec
681 Provincial Health Authority and met the donor selection criteria for plasma donation in use at
682 Héma-Québec were recruited. They were allowed to donate plasma at least 14 days after
683 complete resolution of COVID-19 symptoms. A volume of 500 mL to 750 mL of plasma was
684 collected by plasmapheresis (TRIMA Accel®, Terumo BCT). Disease severity (date of symptoms
685 onset, end of symptoms, type and intensity of symptoms, need for hospitalization/ICU) was
686 documented for each donor using a questionnaire administered at the time of recruitment.

687 **Mouse Experiments**

688 All experiments were approved by the Institutional Animal Care and Use Committees (IACUC) of
689 and Institutional Biosafety Committee of Yale University (IBSCYU). All the animals were housed
690 under specific pathogen-free conditions in the facilities provided and supported by Yale Animal
691 Resources Center (YARC). hACE2 transgenic B6 mice (heterozygous) were obtained from
692 Jackson Laboratory. 6–8-week-old male and female mice were used for all the experiments. The
693 heterozygous mice were crossed and genotyped to select heterozygous mice for experiments by
694 using the primer sets recommended by Jackson Laboratory.
695

696 **METHOD DETAILS**

697 **SARS-CoV-2 infection and treatment conditions**

698 For all *in vivo* experiments, the 6 to 8 weeks male and female mice were
699 intranasally challenged with 1 x 10^5 FFU SARS-CoV-2_WA1_nLuc, WA1, Delta and Beta VOCs
700 in 25-30 µL volume under anesthesia (0.5 - 5 % isoflurane delivered using precision Dräger
701 vaporizer with oxygen flow rate of 1 L/min). For human convalescent plasma treatment using

bioRxiv preprint doi: https://doi.org/10.1101/2022.06.10.495677; this version posted June 12, 2022. The copyright holder for this preprint (which was not certified by peer review) is the author/funder, who has granted bioRxiv a license to display the preprint in perpetuity. It is made available under aCC-BY-NC-ND 4.0 International license.

prophylaxis regimen, mice were administered 1 ml of indicated plasma intraperitoneally (i.p.), 24 h prior to infection. For therapy, the same amount was administered two-day post infection (2 dpi). For IgG and Ig(M+A)-depletion, the plasma had to be diluted 1:1. Hence 2 ml of the Class-depleted plasma was administered intraperitoneally in two injections, 1 ml each and 1 hr apart. The starting body weight was set to 100 %. For survival experiments, mice were monitored every 8-12 h starting six days after virus challenge. Lethargic and moribund mice or mice that had lost more than 20 % of their body weight were sacrificed and considered to have succumbed to infection for Kaplan-Meier survival plots. Mice were considered to have recovered if they gained back all the lost weight.

IgG and Ig(M+A) depletion of CCP

Selective depletion of IgM, IgA or IgG was done by adsorption on isotype-specific ligands immobilized on sepharose or agarose beads starting with a two-fold dilution of plasma in PBS. IgG and IgA antibodies were depleted from plasma obtained from one recovered COVID-19 patient (CCP6) using Protein G HP Spintrap (GE Healthcare Life Sciences, Buckinghamshire, UK) and Peptide M / Agarose (InvivoGen, San Diego, CA), respectively, according to the manufacturer's instructions with the exception that no elution step for the recovery of the targeted antibodies was done. For IgM depletion, anti-human IgM (μ-chain specific, Sigma, St.Louis, MO) was covalently coupled to NHS Activated Sepharose® 4 Fast Flow (GE Healthcare) at 815 μg/mL of matrix. Depletion was performed according to the manufacturer's instructions with the exception that no elution step for the recovery of the targeted isotype was done. All non-depleted and isotype-depleted samples were filtered on a 0.22 μm Millex GV filter (SLGV013SL, Millipore, Burlington, MA) to ensure sterility for the virus capture and neutralization assays. For the preparation of Ig(M+A) depleted samples, plasmas were depleted sequentially in IgM and then in IgA as described above.

bioRxiv preprint doi: https://doi.org/10.1101/2022.06.10.495677; this version posted June 12, 2022. The copyright holder for this preprint (which was not certified by peer review) is the author/funder, who has granted bioRxiv a license to display the preprint in perpetuity. It is made available under aCC-BY-NC-ND 4.0 International license.

To assess the extent of IgM, IgG and IgA depletion, ELISA were performed on non-depleted as well as IgM/IgA- and IgG-depleted plasma samples. Wells of a 96-well microplate were filled with either goat anti-human IgM (μ-chain specific) at 5 μg/mL, goat anti-human serum IgA (a-chain specific) at 0.3 μg/mL or goat anti-human IgG (γ-chain specific) at 5 μg/mL (all from Jackson ImmunoResearch Laboratories, Inc., West Grove, PA). Microtiter plates were sealed and stored overnight at 2- 8°C. After four (IgA) to six (IgM and IgG) washes with H_2O-0.1% Tween 20 (Sigma), 200 μL of blocking solution (10 mmol/L phosphate buffer, pH 7.4, containing 0.85% NaCl, 0.25% Hammerstein casein (EMD Chemicals Inc., Gibbstown, NJ,) were added to each well to block any remaining binding sites. The blocking solution for the IgG and IgM ELISA also contained 0.05% Tween 20. After 0.5 h (IgA) to 1h (IgM and IgG) incubation at 37°C and washes, samples and the standard curves (prepared with human calibrated standard serum, Cedarlane, Burlington, Canada) were added to the plates in triplicates. Plates were incubated for 1h at 37°C. After washes, 100 μL of either goat anti-human IgA+G+M (H+L) HRP conjugate (1/30 000), goat anti-human IgG (H+L) HRP conjugate (1/30 000) or goat anti-human IgA (a-chain specific) HRP conjugate (1/5000) (all from Jackson ImmunoResearch Laboratories, Inc.) were added and samples were incubated at 37°C for 1h. Wells were washed and bound antibodies were detected by the addition of 100 μL of 3,3′,5,5′-tetramethylbenzimidine (TMB, ScyTek Laboratories, Logan, UT). The enzymatic reaction was stopped by the addition of 100 μL 1 N H2SO4 and the absorbance was measured at 450/630 nm within 5 minutes.

Bioluminescence Imaging (BLI) of SARS-CoV-2 infection

All standard operating procedures and protocols for IVIS imaging of SARS-CoV-2 infected animals under ABSL-3 conditions were approved by IACUC, IBSCYU and YARC. All the imaging was carried out using IVIS Spectrum® (PerkinElmer) in XIC-3 animal isolation chamber (PerkinElmer) that provided biological isolation of anesthetized mice or individual organs during the imaging procedure. All mice were anesthetized via isoflurane inhalation (3 - 5 % isoflurane, oxygen flow rate of 1.5 L/min) prior and during BLI using the XGI-8 Gas Anesthesia System. Prior

bioRxiv preprint doi: https://doi.org/10.1101/2022.06.10.495677; this version posted June 12, 2022. The copyright holder for this preprint (which was not certified by peer review) is the author/funder, who has granted bioRxiv a license to display the preprint in perpetuity. It is made available under aCC-BY-NC-ND 4.0 International license.

to imaging, 100 µL of Nanoluc substrate, furimazine (NanoGlo™, Promega, Madison, WI) diluted 1:40 in endotoxin-free PBS was retroorbitally administered to mice under anesthesia. The mice were then placed into XIC-3 animal isolation chamber (PerkinElmer) pre-saturated with isothesia and oxygen mix. The mice were imaged in both dorsal and ventral position at indicated days post infection. The animals were then imaged again after euthanasia and necropsy by spreading additional 200 µL of substrate on to exposed intact organs. Infected areas identified by carrying out whole-body imaging after necropsy were isolated, washed in PBS to remove residual blood and placed onto a clear plastic plate. Additional droplets of furimazine in PBS (1:40) were added to organs and soaked in substrate for 1-2 min before BLI.

Images were acquired and analyzed with Living Image v4.7.3 *in vivo* software package (Perkin Elmer Inc). Image acquisition exposures were set to auto, with imaging parameter preferences set in order of exposure time, binning, and f/stop, respectively. Images were acquired with luminescent f/stop of 2, photographic f/stop of 8. Binning was set to medium. Comparative images were compiled and batch-processed using the image browser with collective luminescent scales. Photon flux was measured as luminescent radiance (p/sec/cm2/sr). During luminescent threshold selection for image display, luminescent signals were regarded as background when minimum threshold setting resulted in displayed radiance above non-tissue-containing or known uninfected regions. To determine the pattern of virus spread, the image sequences were acquired every day following administration of SARS-CoV-2-nLuc (i.n). Image sequences were assembled and converted to videos using Image J.

Focus forming assay

Titers of virus stocks was determined by standard plaque assay. Briefly, the 4 x 10^5 Vero-E6 cells were seeded on 12-well plate. 24 h later, the cells were infected with 200 µL of serially diluted virus stock. After 1 hour, the cells were overlayed with 1ml of pre-warmed 0.6% Avicel (RC-581 FMC BioPolymer) made in complete RPMI medium. Plaques were resolved at 48 h post

bioRxiv preprint doi: https://doi.org/10.1101/2022.06.10.495677; this version posted June 12, 2022. The copyright holder for this preprint (which was not certified by peer review) is the author/funder, who has granted bioRxiv a license to display the preprint in perpetuity. It is made available under aCC-BY-NC-ND 4.0 International license.

infection by fixing in 10 % paraformaldehyde for 15 min followed by staining for 20 min with 0.2 % crystal violet made in 20 % ethanol. Plates were rinsed in water to visualize plaques.

Measurement of viral burden

Indicated organs (nasal cavity, brain, lungs) from infected or uninfected mice were collected, weighed, and homogenized in 1 mL of serum free RPMI media containing penicillin-streptomycin and homogenized in 2 mL tube containing 1.5 mm Zirconium beads with BeadBug 6 homogenizer (Benchmark Scientific, TEquipment Inc). Virus titers were measured using three highly correlative methods. Frist, the total RNA was extracted from homogenized tissues using RNeasy plus Mini kit (Qiagen Cat # 74136), reverse transcribed with iScript advanced cDNA kit (Bio-Rad Cat #1725036) followed by a SYBR Green Real-time PCR assay for determining copies of SARS-CoV-2 N gene RNA using primers SARS-CoV-2 N F: 5'-ATGCTGCAATCGTGCTACAA-3' and SARS-CoV-2 N R: 5'-GACTGCCGCCTCTGCTC-3'.

Second, serially diluted clarified tissue homogenates were used to infect Vero-E6 cell culture monolayer. The titers per gram of tissue were quantified using standard plaque forming assay described above. Third, we used Nanoluc activity as a shorter surrogate for plaque assay. Infected cells were washed with PBS and then lysed using 1X Passive lysis buffer. The lysates transferred into a 96-well solid white plate (Costar Inc) and Nanoluc activity was measured using Tristar multiwell Luminometer (Berthold Technology, Bad Wildbad, Germany) for 2.5 seconds by adding 20 µl of Nano-Glo® substrate in nanoluc assay buffer (Promega Inc, WI, USA). Uninfected monolayer of Vero cells treated identically served as controls to determine basal luciferase activity to obtain normalized relative light units. The data were processed and plotted using GraphPad Prism 8 v8.4.3.

Analyses of signature inflammatory cytokines mRNA expression

Brain and lung samples were collected from mice at the time of necropsy. Approximately, 20 mg of tissue was suspended in 500 µL of RLT lysis buffer, and RNA was extracted using RNeasy plus Mini kit (Qiagen Cat # 74136), reverse transcribed with iScript advanced cDNA kit (Bio-Rad

bioRxiv preprint doi: https://doi.org/10.1101/2022.06.10.495677; this version posted June 12, 2022. The copyright holder for this preprint (which was not certified by peer review) is the author/funder, who has granted bioRxiv a license to display the preprint in perpetuity. It is made available under aCC-BY-NC-ND 4.0 International license.

Cat #1725036). To determine mRNA copy numbers of signature inflammatory cytokines, multiplex qPCR was conducted using iQ Multiplex Powermix (Bio Rad Cat # 1725848) and PrimePCR Probe Assay mouse primers FAM-GAPDH, HEX-IL6, TEX615-CCL2, Cy5-CXCL10, and Cy5.5-IFNgamma. The reaction plate was analyzed using CFX96 touch real time PCR detection system. Scan mode was set to all channels. The PCR conditions were 95 °C 2 min, 40 cycles of 95 °C for 10 s and 60 °C for 45 s, followed by a melting curve analysis to ensure that each primer pair resulted in amplification of a single PCR product. mRNA copy numbers of *Il6, Ccl2, Cxcl10 and Ifng* in the cDNA samples of infected mice were normalized to *Gapdh* mRNA with the formula ΔC_t(target gene)=C_t(target gene)-C_t(*Gapdh*). The fold increase was determined using $2^{-\Delta\Delta Ct}$ method comparing treated mice to uninfected controls.

Antibody depletion of immune cell subsets

Macrophages and neutrophils were depleted during using anti-CSF1R (BioXcell; clone AFS98; 20 mg/kg body weight) (Bauche et al., 2018) and anti-Ly6G (clone: 1A8; 20 mg/kg body weight) (Moynihan et al., 2016) respectively. The mAbs were administered to mice by i.p injection every two days starting at -2 dpi for during CCP prophylaxis or 0 dpi for CCP therapy. Rat IgG2a mAb (BioXCell; clone C1.18.4; 20 mg/kg body weight) or human IgG1 mAb (BioXCell; 12.5 mg/kg body weight) was used as isotype control. The mice were sacrificed and bled 2-3 days after antibody administration or at necropsy to ascertain depletion of desired population.

Flow Cytometric Analyses for Immune cell depletion

For analysis of neutrophil depletion, peripheral blood was collected 2-3 days after administration of depleting antibodies. Erythrocytes were lysed with eBioscience 1X RBC lysis buffer (Invitrogen), PBMCs fixed with 4 % PFA and quenched with PBS containing 0.1M glycine. PFA-fixed cells PBMCs were resuspended and blocked in Cell Staining buffer (BioLegend Inc.) containing Fc blocking antibody against CD16/CD32 (BioLegend Inc) before staining with antibodies. Neutrophils were identified as $CD45^+CD11b^+Ly6G^+$ cells using APC Rat anti-mouse CD45 (30-F11), PE anti-mouse CD11b (M1/70) APC/Cy7 and anti-mouse Ly-6G (1A8) antibodies

bioRxiv preprint doi: https://doi.org/10.1101/2022.06.10.495677; this version posted June 12, 2022. The copyright holder for this preprint (which was not certified by peer review) is the author/funder, who has granted bioRxiv a license to display the preprint in perpetuity. It is made available under aCC-BY-NC-ND 4.0 International license.

For analyses of macrophage depletion, lung tissue was harvested 2 days after administration of antibodies. The tissue was minced and incubated in Hanks' Balanced Salt Solution containing Dispase (5 U/mL; STEMCELL technologies), Liberase TL (0.2 mg/ml, Sigma-Aldrich) and DNase I (100 mg/ml, Roche) at 37°C for 1 h and passed through a 70 µm cell strainer (Falcon, Cat # 352350). The single cell suspension was fixed in BD Cytofix/Cytoperm buffer and stained in BD Cytoperm buffer containing Fc blocking antibody against CD16/CD32 (BioLegend Inc). Macrophages were identified as $CD45^{+}CD11b^{+}Ly6G^{-}L6C^{-}CD68^{+}$ population using Alexa 488 Rat anti-mouse CD45 (30-F11), PE anti-mouse CD11b (M1/70) APC/Cy7 and anti-mouse Ly-6G (1A8), APC/Cy7 anti-mouse Ly-6C (HK1.4) and Alexa 647 anti-mouse CD68 (FA-11) antibodies. Data were acquired on an Accuri C6 (BD Biosciences) and were analyzed with Accuri C6 software. 100,000 – 200,000 viable cells were acquired for each sample. FlowJo software (Treestar) was used to generate FACS plot

Antibody dependent cellular cytotoxicity (ADCC) assay

This assay was previously described (Anand et al., 2021; Beaudoin-Bussieres et al., 2021). Briefly, for evaluation of anti-SARS-CoV-2 antibody-dependent cellular cytotoxicity (ADCC) activity, parental CEM.NKr CCR5+ cells were mixed at a 1:1 ratio with CEM.NKr cells stably expressing a GFP-tagged full length SARS-CoV-2 Spike (CEM.NKr.SARS-CoV-2.Spike cells). These cells were stained for viability (Aqua fluorescent reactive dye, Invitrogen) and with a cellular dye (cell proliferation dye eFluor670; Thermo Fisher Scientific) and subsequently used as target cells. Overnight rested PBMCs were stained with another cellular marker (cell proliferation dye eFluor450; Thermo Fisher Scientific) and used as effector cells. Stained target and effector cells were mixed at a ratio of 1:10 in 96-well V-bottom plates. Plasma (1/500 dilution) was added to the appropriate wells. Monoclonal antibodies CR3022 and CV3-13 were also included (1 µg/mL) in each experiment as a positive control. The plates were subsequently centrifuged for 1 min at 300 x g, and incubated at 37°C, 5% CO_2 for 5 hours and then fixed in a 2% PBS-formaldehyde solution. ADCC activity was calculated using the formula: [(% of GFP+ cells in Targets plus

bioRxiv preprint doi: https://doi.org/10.1101/2022.06.10.495677; this version posted June 12, 2022. The copyright holder for this preprint (which was not certified by peer review) is the author/funder, who has granted bioRxiv a license to display the preprint in perpetuity. It is made available under aCC-BY-NC-ND 4.0 International license.

Effectors) - (% of GFP+ cells in Targets plus Effectors plus plasma/antibody)]/(% of GFP+ cells in Targets) x 100 by gating on transduced live target cells. All samples were acquired on an LSRII cytometer (BD Biosciences) and data analysis was performed using FlowJo v10.7.1 (Tree Star).

Flow cytometry analysis of the different anti-Spike isotypes.

For evaluation of the different antibody isotypes (IgG, IgM, IgA and Total Ig) targeting the SARS-CoV-2 Spike, CEM.NKr cells stably expressing a GFP-tagged full length SARS-CoV-2 Spike and CEM.NKr CCR5+ parental cells were stained for 45 minutes at 25°C with plasma CCP-6, plasma CCP-6 depleted in IgG and plasma CCP-6 depleted in IgA and IgM (1/500). Cells were then washed and further stained with a viability dye staining (Aqua fluorescent reactive dye, Invitrogen) and specific secondary antibodies targeting IgGs (Alexa Fluor® 647 anti-human IgG Fc, BioLegend), IgMs (Alexa Fluor® 647-conjugated AffiniPure Goat Anti-Human IgM, Fc5μ Fragment Specific, Jackson ImmunoResearch), IgAs (Alexa Fluor® 647-conjugated AffiniPure Goat Anti-Human Serum IgA, α Chain Specific, Jackson ImmunoResearch) or Total Igs (Alexa Fluor® 647-conjugated AffiniPure Goat Anti-Human IgA + IgG + IgM (H+L), Jackson ImmunoResearch) for 20 minutes at 25°C. The cells were then washed and fixed in a 2% PBS-Formaldehyde solution. The percentage of transduced cells (GFP+ cells) was determined by gating on the living cell population based on the viability dye staining (Aqua fluorescent reactive dye, Invitrogen). Non-specific staining was evaluated using CEM.NKr CCR5+ parental cells and subtracted from the staining on the live GFP+ cells in the CEM.NKr.Spike cells. Samples were acquired on an LSRII cytometer (BD Biosciences) and data analysis was performed using FlowJo v10.7.1 (Tree Star).

Pseudovirus neutralization assay

To produce the pseudoviruses, 293T cells were transfected with the lentiviral vector pNL4.3 R-E-Luc (NIH AIDS Reagent Program) and a plasmid encoding for the indicated S glycoprotein (D614G) at a ratio of 10:1. Two days post-transfection, cell supernatants were harvested and stored at -80°C until use. For the neutralization assay, 293T-ACE2 target cells were seeded at a

bioRxiv preprint doi: https://doi.org/10.1101/2022.06.10.495677; this version posted June 12, 2022. The copyright holder for this preprint (which was not certified by peer review) is the author/funder, who has granted bioRxiv a license to display the preprint in perpetuity. It is made available under aCC-BY-NC-ND 4.0 International license.

density of 1×104 cells/well in 96-well luminometer-compatible tissue culture plates (Perkin Elmer) 24h before infection. Pseudoviral particles were incubated with several plasma dilutions (1/50; 1/250; 1/1250; 1/6250; 1/31250) for 1h at 37°C and were then added to the target cells followed by incubation for 48h at 37°C. Then, cells were lysed by the addition of 30 µL of passive lysis buffer (Promega) followed by one freeze-thaw cycle. An LB942 TriStar luminometer (Berthold Technologies) was used to measure the luciferase activity of each well after the addition of 100 µL of luciferin buffer (15mM MgSO4, 15mM KPO4 [pH 7.8], 1mM ATP, and 1mM dithiothreitol) and 50 µL of 1mM d-luciferin potassium salt (Prolume). The neutralization half-maximal inhibitory dilution (ID50) represents the plasma dilution to inhibit 50% of the infection of 293T-ACE2 cells by pseudoviruses.

SARS-CoV-2 neutralization assay

Serial two-fold dilutions of heat inactivated (56°C for 30 min) CCPs (1:4, 1:16, 1:64, 1:256, 1:1024) were prepared in triplicates in a volume of 50 µL. 50 µL of WA1, Delta and Beta VOCs (a virus concentration to generate 30-50 plaques per well in six well plate) was mixed with diluted plasma and incubated for 1 h at 37°C. The virus-plasma mixes were then added to Vero E6 cells (7.5 × 10^5 cells/well) seeded 24 h earlier, in 6-well tissue culture plates and allowed to interact with cells for 1 h. The cells were then overlayed with 1 mL of pre-warmed 0.6 % Avicel (RC-581 FMC BioPolymer) made in complete RPMI medium. Plaques were resolved after 72 h by fixing cells in 10 % paraformaldehyde for 15 min followed by staining for 15 minutes with 0.2 % crystal violet made in 20 % ethanol. Plates were rinsed in water to visualize FFU. The FFU counts from virus samples without antibody incubation were set to 100% (30-50 FFU/well). IC_{50} was calculated by plotting the log (plasma dilution) vs normalized FFUs and using non-linear fit option in GraphPad Prism.

Quantification and Statistical Analysis

Data were analyzed and plotted using GraphPad Prism software (La Jolla, CA, USA). Statistical significance for pairwise comparisons were derived by applying non-parametric Mann-Whitney

bioRxiv preprint doi: https://doi.org/10.1101/2022.06.10.495677; this version posted June 12, 2022. The copyright holder for this preprint (which was not certified by peer review) is the author/funder, who has granted bioRxiv a license to display the preprint in perpetuity. It is made available under aCC-BY-NC-ND 4.0 International license.

test (two-tailed). To obtain statistical significance for survival curves, grouped data were compared by log-rank (Mantel-Cox) test. To obtain statistical significance for grouped data we employed 2-way ANOVA followed by Tukey's multiple comparison tests. p values lower than 0.05 were considered statistically significant. P values were indicated as $*$, $p < 0.05$; $**$, $p < 0.01$; $***$, $p < 0.001$; $****$, $p < 0.0001$.

Schematics

Schematics for showing experimental design in figures were created with BioRender.com.

bioRxiv preprint doi: https://doi.org/10.1101/2022.06.10.495677; this version posted June 12, 2022. The copyright holder for this preprint (which was not certified by peer review) is the author/funder, who has granted bioRxiv a license to display the preprint in perpetuity. It is made available under aCC-BY-NC-ND 4.0 International license.

Supplementary Figure Legends

Figure S1. CCP Efficacy During Prophylaxis and Therapy in K18-hACE2 Mice Against Lethal SARS-CoV-2 Challenge. Related to Figure 2

(A, B, G, H) *Ex vivo* imaging of indicated organs and quantification of nLuc signal as flux(photons/sec) after necropsy for an experiment shown in Figure 2A (CCP prophylaxis) and 2G (CCP therapy)

(C, I) Fold change in SARS-CoV-2 nucleocapsid (N gene) expression in brain, lung and nose tissues for experiment as in Figure 2 A and G. The data were normalized to *Gapdh* mRNA expression in the same sample and that in non-infected mice after necropsy.

(D, J) Viral loads (nLuc activity/mg) from indicated tissue using Vero E6 cells as targets for experiment as in Figure 2 A and G. Undetectable virus amounts were set to 1.

(E, F, K, L) Fold change in cytokine mRNA expression in brain and lung tissues for experiment as in Figure 2 A and G. The data were normalized to *Gapdh* mRNA expression in the same sample and that in non-infected mice after necropsy.

Viral loads (D, J) and inflammatory cytokine profile (E, F, K, L) were determined after necropsy for mice that succumb to infection at 6 dpi and for surviving mice at 10 dpi (CCP prophylaxis) or 16 dpi (CCP therapy).

Grouped data in (B-F) and (H-L) were analyzed by 2-way ANOVA followed by Tukey's multiple comparison tests. Statistical significance for group comparisons to isotype are shown in black, with CCP-2 are shown in green, and with CCP-6 are shown in cyan. $*$, $p < 0.05$; $**$, $p < 0.01$; $***$, $p < 0.001$; $****$, $p < 0.0001$; Mean values ± SD are depicted.

Figure S2. Immuno-depletion of Neutrophils and Macrophages does not Influence SARS-CoV-2 Replication in K18-hACE2 Mice. Related to Figure 3

bioRxiv preprint doi: https://doi.org/10.1101/2022.06.10.495677; this version posted June 12, 2022. The copyright holder for this preprint (which was not certified by peer review) is the author/funder, who has granted bioRxiv a license to display the preprint in perpetuity. It is made available under aCC-BY-NC-ND 4.0 International license.

(A, B) Representative FACS plots showing the gating strategy to identify neutrophils ($CD45^+CD11b^+Ly6G^+$) (n= 8; two experiments) and quantification to ascertain their depletion in blood of indicated groups of mice.

(C, D) Representative FACS plots showing the gating strategy to identify tissue resident macrophages in lungs ($CD45^+$ $CD11b^+Ly6G^-Ly6C^-CD68^+$) (n=8; two experiments) and quantification to ascertain their depletion in single cell suspensions of lung tissue in indicated groups of mice.

(B, D): Non-parametric Mann-Whitney test; $*$, $p < 0.05$; $**$, $p < 0.01$; $***$, $p < 0.001$; $****$, $p < 0.0001$; Mean values ± SD are depicted.

(E) Experimental design to test effect of macrophages ($CD45^+Ly6G^-Ly6C^-CD11b^+CD68^+$) and neutrophils ($CD45^+CD11b^+Ly6G^+$) depletion in K18-hACE2 mice challenged with SARS-CoV-2-nLuc (1×10^5 FFU). αCSFR-1 or αLy6G mAbs (i.p., 20 mg/kg body weight) were used to deplete macrophages or neutrophils respectively every 48h starting at -2 dpi. Rat isotype mAb treated cohorts served as controls (Iso). Animals were followed by non-invasive BLI every 2 days as indicated.

(F) Representative BLI images of SARS-CoV-2-nLuc-infected mice in ventral (v) and dorsal (d) positions for experiment as in E. Scale bars denote radiance (photons/sec/cm^2/steradian).

(G, H) Temporal quantification of nLuc signal as flux (photons/sec) computed non-invasively.

(I) Temporal changes in mouse body weight with initial body weight set to 100% for an experiment shown in E.

(J) Kaplan-Meier survival curves of mice (n = 4 per group; two experiments) for experiment as in E.

Figure S3. Macrophage and Neutrophil Depletion Compromises CCP-mediated Protection during Therapy Related to Figure 4

bioRxiv preprint doi: https://doi.org/10.1101/2022.06.10.495677; this version posted June 12, 2022. The copyright holder for this preprint (which was not certified by peer review) is the author/funder, who has granted bioRxiv a license to display the preprint in perpetuity. It is made available under aCC-BY-NC-ND 4.0 International license.

(A-B) *Ex vivo* imaging of indicated organs and quantification of nLuc signal as flux (photons/sec) after necropsy in K18-hACE2 mice for an experiment shown in Figure 4A

(C) Fold change in SARS-CoV-2 nucleocapsid (N gene) expression in brain, lung and nose tissues. The data were normalized to *Gapdh* mRNA expression in the same sample and that in non-infected mice after necropsy.

Grouped data in (B-C), were analyzed by 2-way ANOVA followed by Tukey's multiple comparison tests. Statistical significance for group comparisons to isotype control are shown in black, with CCP-6-treated neutrophil-depleted cohorts are shown in red, CCP-6-treated macrophage-depleted cohorts are shown in green and with CCP-treated cohorts are shown in cyan. $*$, $p < 0.05$; $**$, $p < 0.01$; $***$, $p < 0.001$; $****$, $p < 0.0001$; Mean values ± SD are depicted. See also Figure 4.

Figure S4. Characterization of isotype-depleted CCP-6. Related to Figure 5

(A) Evaluation of indicated Ig class concentration in complete and depleted CCP-6 using ELISA. The relative concentration (%) of each class in the different fractions is shown above the bars.

(B) Levels of Spike-specific denoted antibody classes in complete or depleted CCP-6 fractions, measured by flow cytometry.

(C) Normalized *in vitro* ADCC activity in complete and depleted CCP-6 fractions evaluated using CEM.NKr cells:CEM.NKr.Spike cells (1:1) as targets and PBMCs from an uninfected donor as effectors.

(D) *In vitro* neutralization of Spike-decorated lenti-pseudoviral particles by complete and depleted CCP-6 fractions.

(B-D) Undepleted CCP-6 plasma was used for normalizations and set to 100% Mean values ± SD from 3 experiments or replicates is depicted.

bioRxiv preprint doi: https://doi.org/10.1101/2022.06.10.495677; this version posted June 12, 2022. The copyright holder for this preprint (which was not certified by peer review) is the author/funder, who has granted bioRxiv a license to display the preprint in perpetuity. It is made available under aCC-BY-NC-ND 4.0 International license.

Figure S5 Neutrophils Contribute to Polyclonal IgG-mediated Protection During Prophylaxis in SARS-CoV-2-infected K18-hACE2 Mice. Related to Figure 5

(A-B) *Ex vivo* imaging of indicated organs and quantification of nLuc signal as flux(photons/sec) after necropsy for an experiment shown in Figure 5A

(C) Fold change in SARS-CoV-2 nucleocapsid (N gene) expression in brain, lung and nose tissues. The data were normalized to *Gapdh* mRNA expression in the same sample and that in non-infected mice after necropsy.

Grouped data in (B-C), were analyzed by 2-way ANOVA followed by Tukey's multiple comparison tests. Statistical significance for group comparisons to isotype control are shown in black, with IgG-equated CCP-6 are shown in cyan, with convalescent plasma IgG depleted CCP-6 are shown in red, with Ig(M+A)-depleted CCP-6 are shown in green and with Ig(M+A)-depleted CCP-6 under neutrophil depletion are shown in orange. $*$, $p < 0.05$; $**$, $p < 0.01$; $***$, $p < 0.001$; $****$, $p < 0.0001$; Mean values ± SD are depicted.

Figure S6. Polyclonal IgG and Ig(M+A) Contribute to Protection During CCP Therapy. Related to Figure 6

(A-B) *Ex vivo* imaging of indicated organs and quantification of nLuc signal as flux(photons/sec) after necropsy for an experiment shown in Figure 6A

(C) Fold change in SARS-CoV-2 nucleocapsid (N gene) expression in brain, lung and nose tissues. The data were normalized to *Gapdh* mRNA expression in the same sample and that in non-infected mice after necropsy.

Grouped data in (B-C), were analyzed by 2-way ANOVA followed by Tukey's multiple comparison tests. Statistical significance for group comparisons to isotype control are shown in black, with IgG-equated CCP-6 are shown in cyan, with IgG-depleted CCP-6 are shown in red and with Ig(M+A)-depleted CCP-6 are shown in green $*$, $p < 0.05$; $**$, $p < 0.01$; $***$, $p < 0.001$; $****$, $p < 0.0001$; Mean values ± SD are depicted.

bioRxiv preprint doi: https://doi.org/10.1101/2022.06.10.495677; this version posted June 12, 2022. The copyright holder for this preprint (which was not certified by peer review) is the author/funder, who has granted bioRxiv a license to display the preprint in perpetuity. It is made available under aCC-BY-NC-ND 4.0 International license.

References

Anand, S.P., Prevost, J., Nayrac, M., Beaudoin-Bussieres, G., Benlarbi, M., Gasser, R., Brassard, N., Laumaea, A., Gong, S.Y., Bourassa, C., et al. (2021). Longitudinal analysis of humoral immunity against SARS-CoV-2 Spike in convalescent individuals up to 8 months post-symptom onset. Cell Rep Med. 2(6), 100290. DOI: 10.1016/j.xcrm.2021.100290.

Basheer, M., Saad, E., Shlezinger, D., and Assy, N. (2021). Convalescent Plasma Reduces Mortality and Decreases Hospitalization Stay in Patients with Moderate COVID-19 Pneumonia. Metabolites. 11(11). DOI: 10.3390/metabo11110761.

Bauche, D., Joyce-Shaikh, B., Jain, R., Grein, J., Ku, K.S., Blumenschein, W.M., Ganal-Vonarburg, S.C., Wilson, D.C., McClanahan, T.K., Malefyt, R.W., et al. (2018). LAG3(+) Regulatory T Cells Restrain Interleukin-23-Producing CX3CR1(+) Gut-Resident Macrophages during Group 3 Innate Lymphoid Cell-Driven Colitis. Immunity. 49(2), 342-352 e345. DOI: 10.1016/j.immuni.2018.07.007.

Beaudoin-Bussieres, G., Chen, Y., Ullah, I., Prevost, J., Tolbert, W.D., Symmes, K., Ding, S., Benlarbi, M., Gong, S.Y., Tauzin, A., et al. (2022). A Fc-enhanced NTD-binding non-neutralizing antibody delays virus spread and synergizes with a nAb to protect mice from lethal SARS-CoV-2 infection. Cell Rep. 38(7), 110368. Published online 20220125 DOI: 10.1016/j.celrep.2022.110368.

Beaudoin-Bussieres, G., Richard, J., Prevost, J., Goyette, G., and Finzi, A. (2021). A new flow cytometry assay to measure antibody-dependent cellular cytotoxicity against SARS-CoV-2 Spike-expressing cells. STAR Protoc. 2(4), 100851. DOI: 10.1016/j.xpro.2021.100851.

Begin, P., Callum, J., Jamula, E., Cook, R., Heddle, N.M., Tinmouth, A., Zeller, M.P., Beaudoin-Bussieres, G., Amorim, L., Bazin, R., et al. (2021). Convalescent plasma for hospitalized patients with COVID-19: an open-label, randomized controlled trial. Nat Med. 27(11), 2012-2024. DOI: 10.1038/s41591-021-01488-2.

Beraud, M., Goodhue Meyer, E., Lozano, M., Bah, A., Vassallo, R., and Brown, B.L. (2022). Lessons learned from the use of convalescent plasma for the treatment of COVID-19 and specific considerations for immunocompromised patients. Transfus Apher Sci. 103355. DOI: 10.1016/j.transci.2022.103355.

Cao, H., and Shi, Y. (2020). Convalescent plasma: possible therapy for novel coronavirus disease 2019. Transfusion. 60(5), 1078-1083. DOI: 10.1111/trf.15797.

Cao, Y., Wang, J., Jian, F., Xiao, T., Song, W., Yisimayi, A., Huang, W., Li, Q., Wang, P., An, R., et al. (2022). Omicron escapes the majority of existing SARS-CoV-2 neutralizing antibodies. Nature. 602(7898), 657-663. DOI: 10.1038/s41586-021-04385-3.

Casadevall, A., and Scharff, M.D. (1995). Return to the past: the case for antibody-based therapies in infectious diseases. Clin Infect Dis. 21(1), 150-161. DOI: 10.1093/clinids/21.1.150.

Dispinseri, S., Secchi, M., Pirillo, M.F., Tolazzi, M., Borghi, M., Brigatti, C., De Angelis, M.L., Baratella, M., Bazzigaluppi, E., Venturi, G., et al. (2021). Neutralizing antibody responses to SARS-CoV-2 in symptomatic COVID-19 is persistent and critical for survival. Nat Commun. 12(1), 2670. DOI: 10.1038/s41467-021-22958-8.

bioRxiv preprint doi: https://doi.org/10.1101/2022.06.10.495677; this version posted June 12, 2022. The copyright holder for this preprint (which was not certified by peer review) is the author/funder, who has granted bioRxiv a license to display the preprint in perpetuity. It is made available under aCC-BY-NC-ND 4.0 International license.

Gasser, R., Cloutier, M., Prevost, J., Fink, C., Ducas, E., Ding, S., Dussault, N., Landry, P., Tremblay, T., Laforce-Lavoie, A., et al. (2021). Major role of IgM in the neutralizing activity of convalescent plasma against SARS-CoV-2. Cell Rep. 34(9), 108790. DOI: 10.1016/j.celrep.2021.108790.

Greaney, A.J., Starr, T.N., and Bloom, J.D. (2022). An antibody-escape estimator for mutations to the SARS-CoV-2 receptor-binding domain. Virus Evol. 8(1), veac021. DOI: 10.1093/ve/veac021.

Gundlapalli, A.V., Salerno, R.M., Brooks, J.T., Averhoff, F., Petersen, L.R., McDonald, L.C., Iademarco, M.F., and Response, C.C.-. (2021). SARS-CoV-2 Serologic Assay Needs for the Next Phase of the US COVID-19 Pandemic Response. Open Forum Infect Dis. 8(1), ofaa555. DOI: 10.1093/ofid/ofaa555.

Gunn, B.M., Lu, R., Slein, M.D., Ilinykh, P.A., Huang, K., Atyeo, C., Schendel, S.L., Kim, J., Cain, C., Roy, V., et al. (2021). A Fc engineering approach to define functional humoral correlates of immunity against Ebola virus. Immunity. 54(4), 815-828 e815. DOI: 10.1016/j.immuni.2021.03.009.

Halfmann, P.J., Iida, S., Iwatsuki-Horimoto, K., Maemura, T., Kiso, M., Scheaffer, S.M., Darling, T.L., Joshi, A., Loeber, S., Singh, G., et al. (2022). SARS-CoV-2 Omicron virus causes attenuated disease in mice and hamsters. Nature. 603(7902), 687-692. DOI: 10.1038/s41586-022-04441-6.
Jennewein, M.F., MacCamy, A.J., Akins, N.R., Feng, J., Homad, L.J., Hurlburt, N.K., Seydoux, E., Wan, Y.H., Stuart, A.B., Edara, V.V., et al. (2021). Isolation and characterization of cross-neutralizing coronavirus antibodies from COVID-19+ subjects. Cell Rep. 36(2), 109353. DOI: 10.1016/j.celrep.2021.109353.

Kaplonek, P., Cizmeci, D., Fischinger, S., Collier, A.R., Suscovich, T., Linde, C., Broge, T., Mann, C., Amanat, F., Dayal, D., et al. (2022a). mRNA-1273 and BNT162b2 COVID-19 vaccines elicit antibodies with differences in Fc-mediated effector functions. Sci Transl Med. 14(645), eabm2311. DOI: 10.1126/scitranslmed.abm2311.

Kaplonek, P., Fischinger, S., Cizmeci, D., Bartsch, Y.C., Kang, J., Burke, J.S., Shin, S.A., Dayal, D., Martin, P., Mann, C., et al. (2022b). mRNA-1273 vaccine-induced antibodies maintain Fc effector functions across SARS-CoV-2 variants of concern. Immunity. 55(2), 355-365 e354. DOI: 10.1016/j.immuni.2022.01.001.

Korley, F.K., Durkalski-Mauldin, V., Yeatts, S.D., Schulman, K., Davenport, R.D., Dumont, L.J., El Kassar, N., Foster, L.D., Hah, J.M., Jaiswal, S., et al. (2021). Early Convalescent Plasma for High-Risk Outpatients with Covid-19. N Engl J Med. 385(21), 1951-1960. DOI: 10.1056/NEJMoa2103784.

Ku, Z., Xie, X., Hinton, P.R., Liu, X., Ye, X., Muruato, A.E., Ng, D.C., Biswas, S., Zou, J., Liu, Y., et al. (2021). Nasal delivery of an IgM offers broad protection from SARS-CoV-2 variants. Nature. 595(7869), 718-723. DOI: 10.1038/s41586-021-03673-2.

Ledford, H. (2020). Antibody therapies could be a bridge to a coronavirus vaccine - but will the world benefit? Nature. 584(7821), 333-334. DOI: 10.1038/d41586-020-02360-y.

Li, W., Chen, Y., Prevost, J., Ullah, I., Lu, M., Gong, S.Y., Tauzin, A., Gasser, R., Vezina, D., Anand, S.P., et al. (2022). Structural basis and mode of action for two broadly neutralizing

bioRxiv preprint doi: https://doi.org/10.1101/2022.06.10.495677; this version posted June 12, 2022. The copyright holder for this preprint (which was not certified by peer review) is the author/funder, who has granted bioRxiv a license to display the preprint in perpetuity. It is made available under aCC-BY-NC-ND 4.0 International license.

antibodies against SARS-CoV-2 emerging variants of concern. Cell Rep. 38(2), 110210. Published online 20211215 DOI: 10.1016/j.celrep.2021.110210.

Liu, D., and Shameem, M. (2022). Antiviral monoclonal antibody cocktails as a modern weapon in combating pandemics. Ther Deliv. 13(2), 67-69. DOI: 10.4155/tde-2021-0079.

Liu, L., Iketani, S., Guo, Y., Chan, J.F., Wang, M., Liu, L., Luo, Y., Chu, H., Huang, Y., Nair, M.S., et al. (2022). Striking antibody evasion manifested by the Omicron variant of SARS-CoV-2. Nature. 602(7898), 676-681. DOI: 10.1038/s41586-021-04388-0.

Ljungquist, O., Lundgren, M., Iliachenko, E., Mansson, F., Bottiger, B., Landin-Olsson, M., Wiken, C., Rosendal, E., Overby, A.K., Wigren, B.J., et al. (2022). Convalescent plasma treatment in severely immunosuppressed patients hospitalized with COVID-19: an observational study of 28 cases. Infect Dis (Lond). 54(4), 283-291. DOI: 10.1080/23744235.2021.2013528.

Lu, L.L., Suscovich, T.J., Fortune, S.M., and Alter, G. (2018). Beyond binding: antibody effector functions in infectious diseases. Nat Rev Immunol. 18(1), 46-61. DOI: 10.1038/nri.2017.106.

Luke, T.C., Kilbane, E.M., Jackson, J.L., and Hoffman, S.L. (2006). Meta-analysis: convalescent blood products for Spanish influenza pneumonia: a future H5N1 treatment? Ann Intern Med. 145(8), 599-609. DOI: 10.7326/0003-4819-145-8-200610170-00139.

Mair-Jenkins, J., Saavedra-Campos, M., Baillie, J.K., Cleary, P., Khaw, F.M., Lim, W.S., Makki, S., Rooney, K.D., Nguyen-Van-Tam, J.S., Beck, C.R., et al. (2015). The effectiveness of convalescent plasma and hyperimmune immunoglobulin for the treatment of severe acute respiratory infections of viral etiology: a systematic review and exploratory meta-analysis. J Infect Dis. 211(1), 80-90. DOI: 10.1093/infdis/jiu396.

McCray, P.B., Jr., Pewe, L., Wohlford-Lenane, C., Hickey, M., Manzel, L., Shi, L., Netland, J., Jia, H.P., Halabi, C., Sigmund, C.D., et al. (2007). Lethal infection of K18-hACE2 mice infected with severe acute respiratory syndrome coronavirus. J Virol. 81(2), 813-821. DOI: 10.1128/JVI.02012-06.

Moynihan, K.D., Opel, C.F., Szeto, G.L., Tzeng, A., Zhu, E.F., Engreitz, J.M., Williams, R.T., Rakhra, K., Zhang, M.H., Rothschilds, A.M., et al. (2016). Eradication of large established tumors in mice by combination immunotherapy that engages innate and adaptive immune responses. Nat Med. 22(12), 1402-1410. DOI: 10.1038/nm.4200.

Park, J.G., Pino, P.A., Akhter, A., Alvarez, X., Torrelles, J.B., and Martinez-Sobrido, L. (2022). Animal Models of COVID-19: Transgenic Mouse Model. Methods Mol Biol. 2452, 259-289. DOI: 10.1007/978-1-0716-2111-0_16.

Patel, K.R., Roberts, J.T., and Barb, A.W. (2019). Multiple Variables at the Leukocyte Cell Surface Impact Fc gamma Receptor-Dependent Mechanisms. Front Immunol. 10, 223. DOI: 10.3389/fimmu.2019.00223.

Pereira, N.A., Chan, K.F., Lin, P.C., and Song, Z. (2018). The "less-is-more" in therapeutic antibodies: Afucosylated anti-cancer antibodies with enhanced antibody-dependent cellular cytotoxicity. MAbs. 10(5), 693-711. DOI: 10.1080/19420862.2018.1466767.

Perreault, J., Tremblay, T., Fournier, M.J., Drouin, M., Beaudoin-Bussieres, G., Prevost, J., Lewin, A., Begin, P., Finzi, A., and Bazin, R. (2020). Waning of SARS-CoV-2 RBD antibodies in

bioRxiv preprint doi: https://doi.org/10.1101/2022.06.10.495677; this version posted June 12, 2022. The copyright holder for this preprint (which was not certified by peer review) is the author/funder, who has granted bioRxiv a license to display the preprint in perpetuity. It is made available under aCC-BY-NC-ND 4.0 International license.

longitudinal convalescent plasma samples within 4 months after symptom onset. Blood. 136(22), 2588-2591. DOI: 10.1182/blood.2020008367.

Pinkus, G.S., and Said, J.W. (1986). Leu-M1 immunoreactivity in nonhematopoietic neoplasms and myeloproliferative disorders. An immunoperoxidase study of paraffin sections. Am J Clin Pathol. 85(3), 278-282. DOI: 10.1093/ajcp/85.3.278.

Planas, D., Saunders, N., Maes, P., Guivel-Benhassine, F., Planchais, C., Buchrieser, J., Bolland, W.H., Porrot, F., Staropoli, I., Lemoine, F., et al. (2022). Considerable escape of SARS-CoV-2 Omicron to antibody neutralization. Nature. 602(7898), 671-675. DOI: 10.1038/s41586-021-04389-z.

Prevost, J., Gasser, R., Beaudoin-Bussieres, G., Richard, J., Duerr, R., Laumaea, A., Anand, S.P., Goyette, G., Benlarbi, M., Ding, S., et al. (2020). Cross-Sectional Evaluation of Humoral Responses against SARS-CoV-2 Spike. Cell Rep Med. 1(7), 100126. DOI: 10.1016/j.xcrm.2020.100126.

Richardson, S.I., Manamela, N.P., Motsoeneng, B.M., Kaldine, H., Ayres, F., Makhado, Z., Mennen, M., Skelem, S., Williams, N., Sullivan, N.J., et al. (2022). SARS-CoV-2 Beta and Delta variants trigger Fc effector function with increased cross-reactivity. Cell Rep Med. 3(2), 100510. DOI: 10.1016/j.xcrm.2022.100510.

Russell, M.W., Moldoveanu, Z., Ogra, P.L., and Mestecky, J. (2020). Mucosal Immunity in COVID-19: A Neglected but Critical Aspect of SARS-CoV-2 Infection. Front Immunol. 11, 611337. DOI: 10.3389/fimmu.2020.611337.

Schafer, A., Muecksch, F., Lorenzi, J.C.C., Leist, S.R., Cipolla, M., Bournazos, S., Schmidt, F., Maison, R.M., Gazumyan, A., Martinez, D.R., et al. (2021). Antibody potency, effector function, and combinations in protection and therapy for SARS-CoV-2 infection in vivo. J Exp Med. 218(3). DOI: 10.1084/jem.20201993.

Seehusen, F., Clark, J.J., Sharma, P., Bentley, E.G., Kirby, A., Subramaniam, K., Wunderlin-Giuliani, S., Hughes, G.L., Patterson, E.I., Michael, B.D., et al. (2022). Neuroinvasion and Neurotropism by SARS-CoV-2 Variants in the K18-hACE2 Mouse. Viruses. 14(5). DOI: 10.3390/v14051020.

Tada, T., Zhou, H., Dcosta, B.M., Samanovic, M.I., Chivukula, V., Herati, R.S., Hubbard, S.R., Mulligan, M.J., and Landau, N.R. (2022). Increased resistance of SARS-CoV-2 Omicron variant to neutralization by vaccine-elicited and therapeutic antibodies. EBioMedicine. 78, 103944. DOI: 10.1016/j.ebiom.2022.103944.

Tartof, S.Y., Slezak, J.M., Puzniak, L., Hong, V., Xie, F., Ackerson, B.K., Valluri, S.R., Jodar, L., and McLaughlin, J.M. (2022). Durability of BNT162b2 vaccine against hospital and emergency department admissions due to the omicron and delta variants in a large health system in the USA: a test-negative case-control study. Lancet Respir Med. DOI: 10.1016/S2213-2600(22)00101-1.

Tauzin, A., Nayrac, M., Benlarbi, M., Gong, S.Y., Gasser, R., Beaudoin-Bussieres, G., Brassard, N., Laumaea, A., Vezina, D., Prevost, J., et al. (2021). A single dose of the SARS-CoV-2 vaccine BNT162b2 elicits Fc-mediated antibody effector functions and T cell responses. Cell Host Microbe. 29(7), 1137-1150 e1136. DOI: 10.1016/j.chom.2021.06.001.

bioRxiv preprint doi: https://doi.org/10.1101/2022.06.10.495677; this version posted June 12, 2022. The copyright holder for this preprint (which was not certified by peer review) is the author/funder, who has granted bioRxiv a license to display the preprint in perpetuity. It is made available under aCC-BY-NC-ND 4.0 International license.

1216 Tay, M.Z., Wiehe, K., and Pollara, J. (2019). Antibody-Dependent Cellular Phagocytosis in
1217 Antiviral Immune Responses. Front Immunol. 10, 332. DOI: 10.3389/fimmu.2019.00332.
1218
1219 Ullah, I., Prevost, J., Ladinsky, M.S., Stone, H., Lu, M., Anand, S.P., Beaudoin-Bussieres, G.,
1220 Symmes, K., Benlarbi, M., Ding, S., et al. (2021). Live imaging of SARS-CoV-2 infection in mice
1221 reveals that neutralizing antibodies require Fc function for optimal efficacy. Immunity. 54(9), 2143-
1222 2158 e2115. DOI: 10.1016/j.immuni.2021.08.015.
1223
1224 van Erp, E.A., Luytjes, W., Ferwerda, G., and van Kasteren, P.B. (2019). Fc-Mediated Antibody
1225 Effector Functions During Respiratory Syncytial Virus Infection and Disease. Front Immunol. 10,
1226 548. DOI: 10.3389/fimmu.2019.00548.
1227
1228 Villa, C.H. (2021). Clinical memorandum for use of COVID-19 Convalescent Plasma EUA 26382,
1229 https://www.fda.gov/media/141480/download
1230
1231 Wang, Z., Lorenzi, J.C.C., Muecksch, F., Finkin, S., Viant, C., Gaebler, C., Cipolla, M., Hoffmann,
1232 H.H., Oliveira, T.Y., Oren, D.A., et al. (2021). Enhanced SARS-CoV-2 neutralization by dimeric
1233 IgA. Sci Transl Med. 13(577). DOI: 10.1126/scitranslmed.abf1555.
1234
1235 Winkler, E.S., Gilchuk, P., Yu, J., Bailey, A.L., Chen, R.E., Chong, Z., Zost, S.J., Jang, H., Huang,
1236 Y., Allen, J.D., et al. (2021). Human neutralizing antibodies against SARS-CoV-2 require intact
1237 Fc effector functions for optimal therapeutic protection. Cell. 184(7), 1804-1820 e1816. DOI:
1238 10.1016/j.cell.2021.02.026.
1239
1240 Writing Committee for the, R.-C.A.P.I., Estcourt, L.J., Turgeon, A.F., McQuilten, Z.K., McVerry,
1241 B.J., Al-Beidh, F., Annane, D., Arabi, Y.M., Arnold, D.M., Beane, A., et al. (2021). Effect of
1242 Convalescent Plasma on Organ Support-Free Days in Critically Ill Patients With COVID-19: A
1243 Randomized Clinical Trial. JAMA. 326(17), 1690-1702. DOI: 10.1001/jama.2021.18178.
1244
1245 Xie, X., Muruato, A., Lokugamage, K.G., Narayanan, K., Zhang, X., Zou, J., Liu, J., Schindewolf,
1246 C., Bopp, N.E., Aguilar, P.V., et al. (2020). An Infectious cDNA Clone of SARS-CoV-2. Cell Host
1247 Microbe. 27(5), 841-848 e843. DOI: 10.1016/j.chom.2020.04.004.
1248
1249 Yamin, R., Jones, A.T., Hoffmann, H.H., Schafer, A., Kao, K.S., Francis, R.L., Sheahan, T.P.,
1250 Baric, R.S., Rice, C.M., Ravetch, J.V., et al. (2021). Fc-engineered antibody therapeutics with
1251 improved anti-SARS-CoV-2 efficacy. Nature. 599(7885), 465-470. DOI: 10.1038/s41586-021-
1252 04017-w.
1253

1254 Zheng, J., Wong, L.R., Li, K., Verma, A.K., Ortiz, M.E., Wohlford-Lenane, C., Leidinger, M.R.,
1255 Knudson, C.M., Meyerholz, D.K., McCray, P.B., Jr., et al. (2021). COVID-19 treatments and
1256 pathogenesis including anosmia in K18-hACE2 mice. Nature. 589(7843), 603-607. DOI:
1257 10.1038/s41586-020-2943-z.

Figure 1

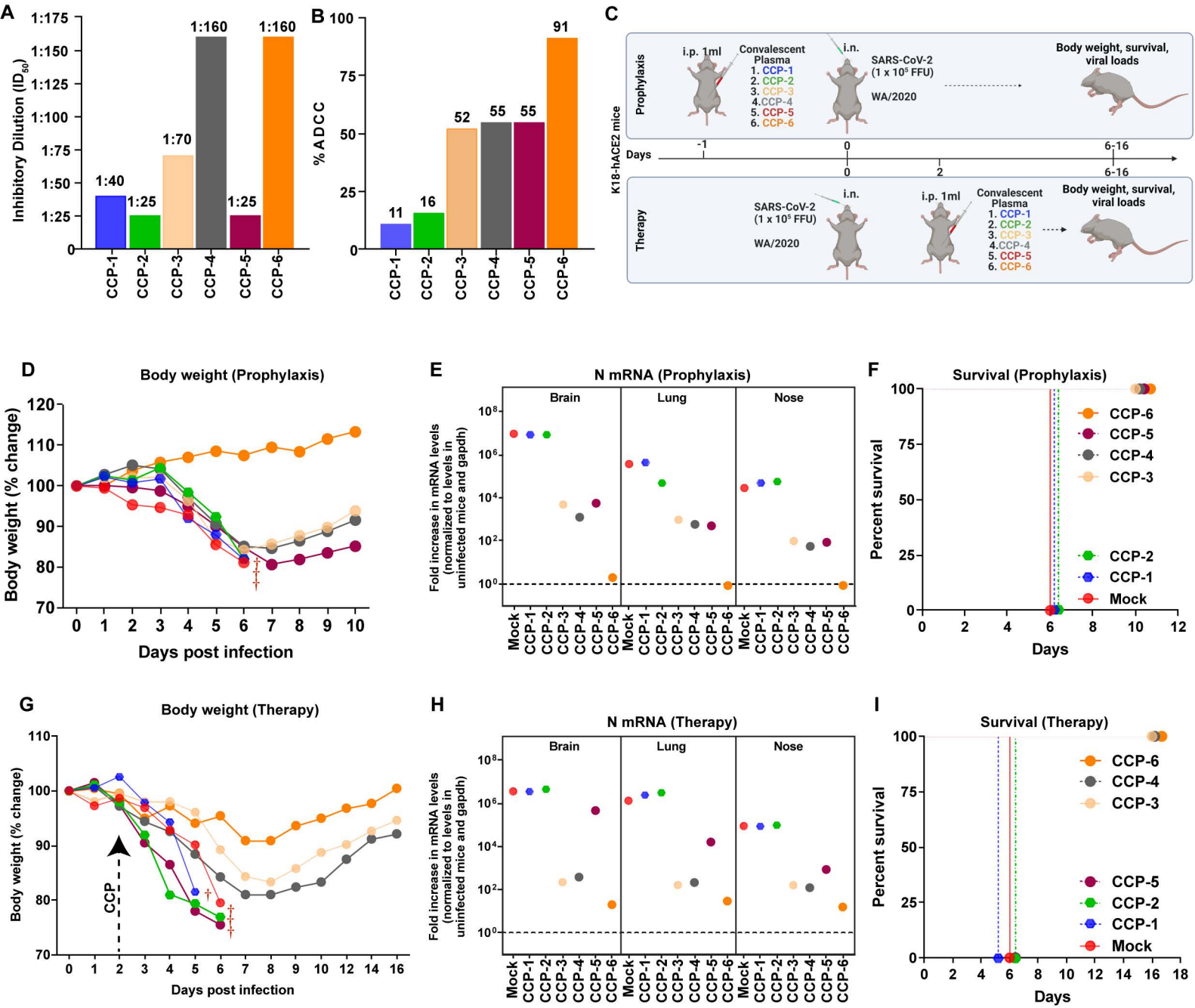
A
Inhibitory Dilution (ID50)
1:175
1:150
1:125
1:100
1:75
1:50
1:25
0
1:40
1:25
1:70
1:160
1:25
1:160
CCP-1
CCP-2
CCP-3
CCP-4
CCP-5
CCP-6
B
% ADCC
100
75
50
25
0
11
16
52
55
55
91
C
K18-hACE2 mice
Prophylaxis
i.p. 1ml
Convalescent Plasma
1. CCP-1
2. CCP-2
3. CCP-3
4.CCP-4
5. CCP-5
6. CCP-6
i.n.
SARS-CoV-2 (1 x 10⁵ FFU)
WA/2020
Body weight, survival, viral loads
Days
-1
0
6-16
0
2
6-16
Therapy
SARS-CoV-2 (1 x 10⁵ FFU)
WA/2020
i.n.
i.p. 1ml
Convalescent Plasma
1. CCP-1
2. CCP-2
3. CCP-3
4.CCP-4
5. CCP-5
6. CCP-6
Body weight, survival, viral loads
D
Body weight (Prophylaxis)
Body weight (% change)
Days post infection
E
N mRNA (Prophylaxis)
Brain
Lung
Nose
Fold increase in mRNA levels (normalized to levels in uninfected mice and gapdh)
Mock
CCP-1
CCP-2
CCP-3
CCP-4
CCP-5
CCP-6
F
Survival (Prophylaxis)
Percent survival
Days
CCP-6
CCP-5
CCP-4
CCP-3
CCP-2
CCP-1
Mock
G
Body weight (Therapy)
Body weight (% change)
CCP
Days post infection
H
N mRNA (Therapy)
Brain
Lung
Nose
Fold increase in mRNA levels (normalized to levels in uninfected mice and gapdh)
I
Survival (Therapy)
Percent survival
Days
CCP-6
CCP-4
CCP-3
CCP-5
CCP-2
CCP-1
Mock

Figure 2

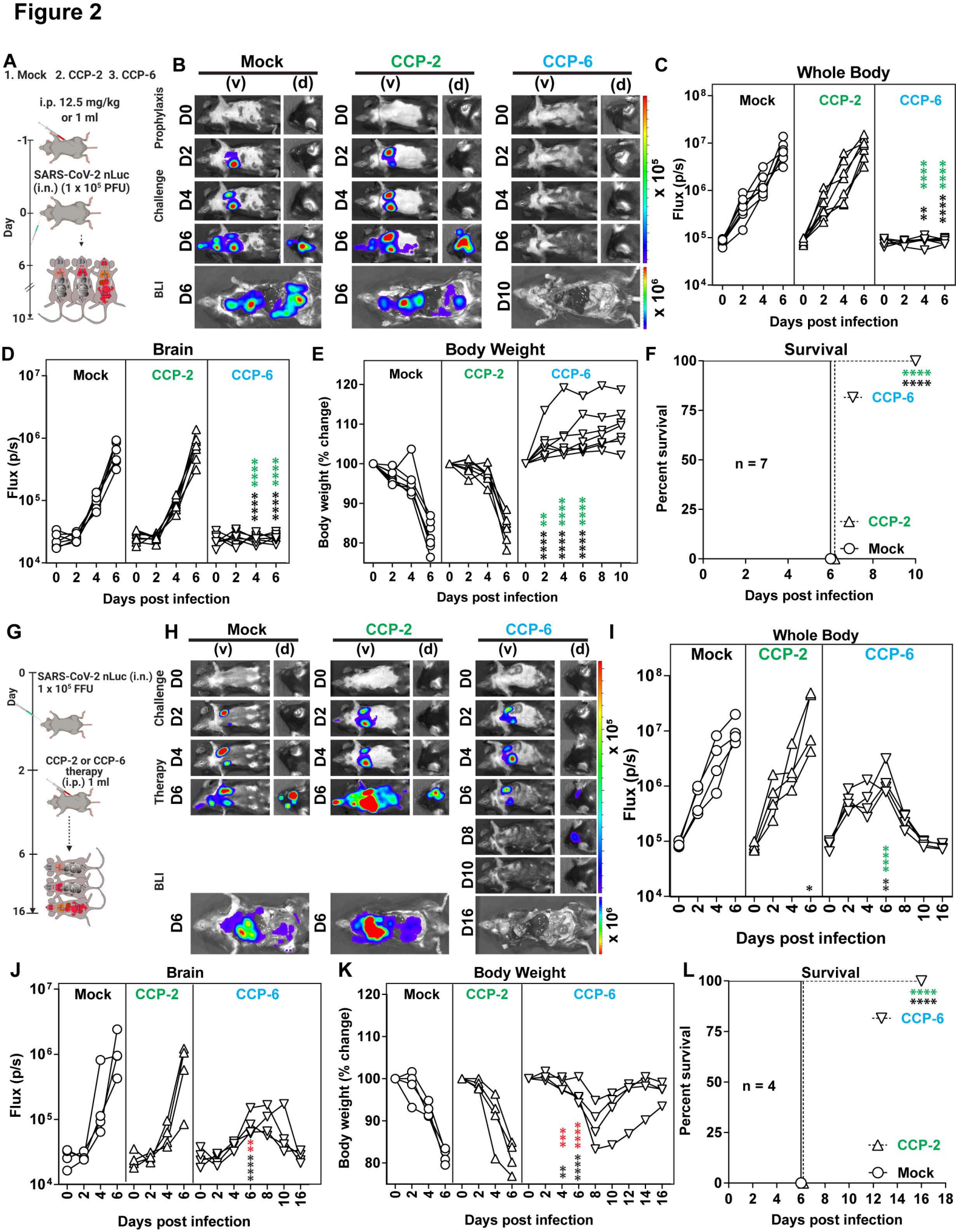
A
1. Mock 2. CCP-2 3. CCP-6
i.p. 12.5 mg/kg or 1 ml
SARS-CoV-2 nLuc (i.n.) (1 x 10^5 PFU)
Day
B
Mock
CCP-2
CCP-6
(v)
(d)
Prophylaxis
Challenge
BLI
D0
D2
D4
D6
D10
x 10^5
x 10^6
C
Whole Body
Flux (p/s)
Days post infection
D
Brain
E
Body Weight
Body weight (% change)
F
Survival
Percent survival
n = 7
G
SARS-CoV-2 nLuc (i.n.) 1 x 10^5 FFU
CCP-2 or CCP-6 therapy (i.p.) 1 ml
Therapy
H
D8
I
J
K
L
n = 4

Figure 3

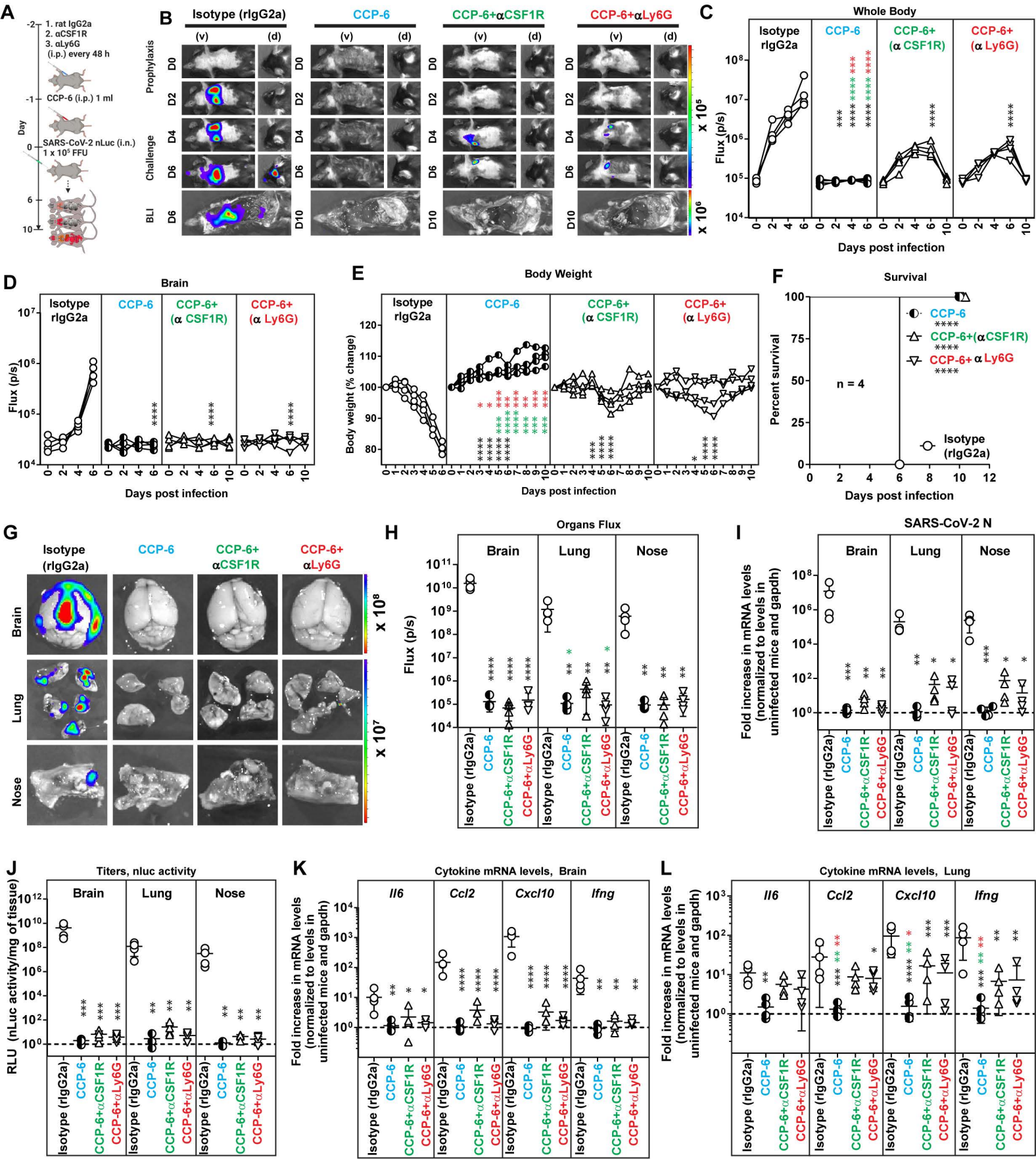
A
1. rat IgG2a
2. αCSF1R
3. αLy6G
(i.p.) every 48 h
CCP-6 (i.p.) 1 ml
SARS-CoV-2 nLuc (i.n.)
1 x 10⁵ FFU
Day
B
Isotype (rIgG2a)
CCP-6
CCP-6+αCSF1R
CCP-6+αLy6G
(v)
(d)
Prophylaxis
Challenge
BLI
x 10⁵
x 10⁶
C
Whole Body
Isotype rIgG2a
CCP-6
CCP-6+ (α CSF1R)
CCP-6+ (α Ly6G)
Flux (p/s)
Days post infection
D
Brain
E
Body Weight
Body weight (% change)
F
Survival
Percent survival
n = 4
CCP-6
CCP-6+(αCSF1R)
CCP-6+ αLy6G
Isotype (rIgG2a)
G
Brain
Lung
Nose
x 10⁸
x 10⁷
H
Organs Flux
Flux (p/s)
I
SARS-CoV-2 N
Fold increase in mRNA levels (normalized to levels in uninfected mice and gapdh)
J
Titers, nluc activity
RLU (nLuc activity/mg of tissue)
K
Cytokine mRNA levels, Brain
Il6
Ccl2
Cxcl10
Ifng
L
Cytokine mRNA levels, Lung

Figure 4

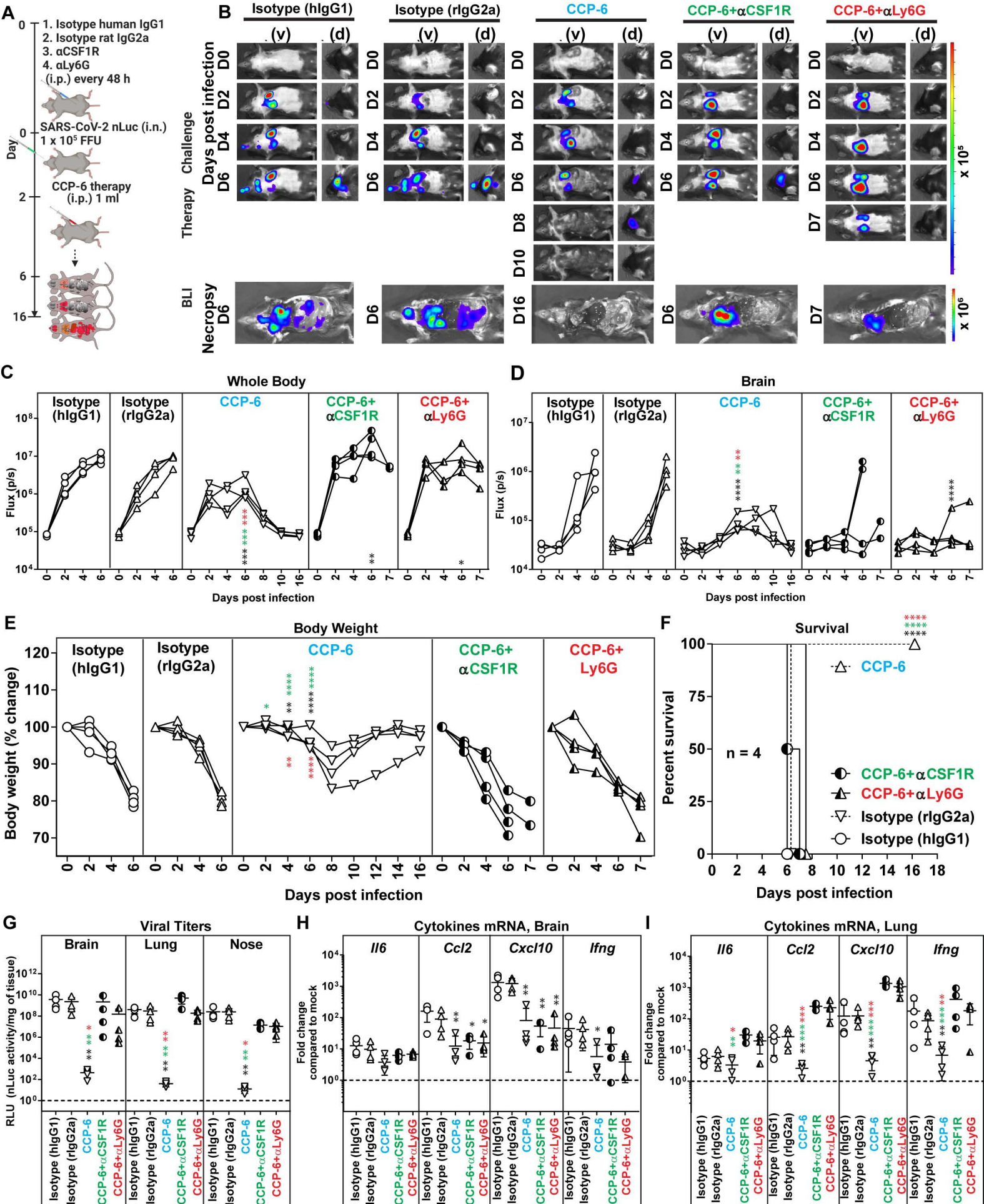
A
1. Isotype human IgG1
2. Isotype rat IgG2a
3. αCSF1R
4. αLy6G
(i.p.) every 48 h
SARS-CoV-2 nLuc (i.n.)
1 x 10^5 FFU
CCP-6 therapy
(i.p.) 1 ml
Day
B
Isotype (hIgG1)
Isotype (rIgG2a)
CCP-6
CCP-6+αCSF1R
CCP-6+αLy6G
(v)
(d)
Days post infection
Challenge
Therapy
BLI
Necropsy
x 10^5
x 10^6
C
Whole Body
Flux (p/s)
Days post infection
D
Brain
E
Body Weight
Body weight (% change)
Days post infection
F
Survival
Percent survival
n = 4
Days post infection
G
Viral Titers
Brain
Lung
Nose
RLU (nLuc activity/mg of tissue)
H
Cytokines mRNA, Brain
Il6
Ccl2
Cxcl10
Ifng
Fold change compared to mock
I
Cytokines mRNA, Lung

Figure 5

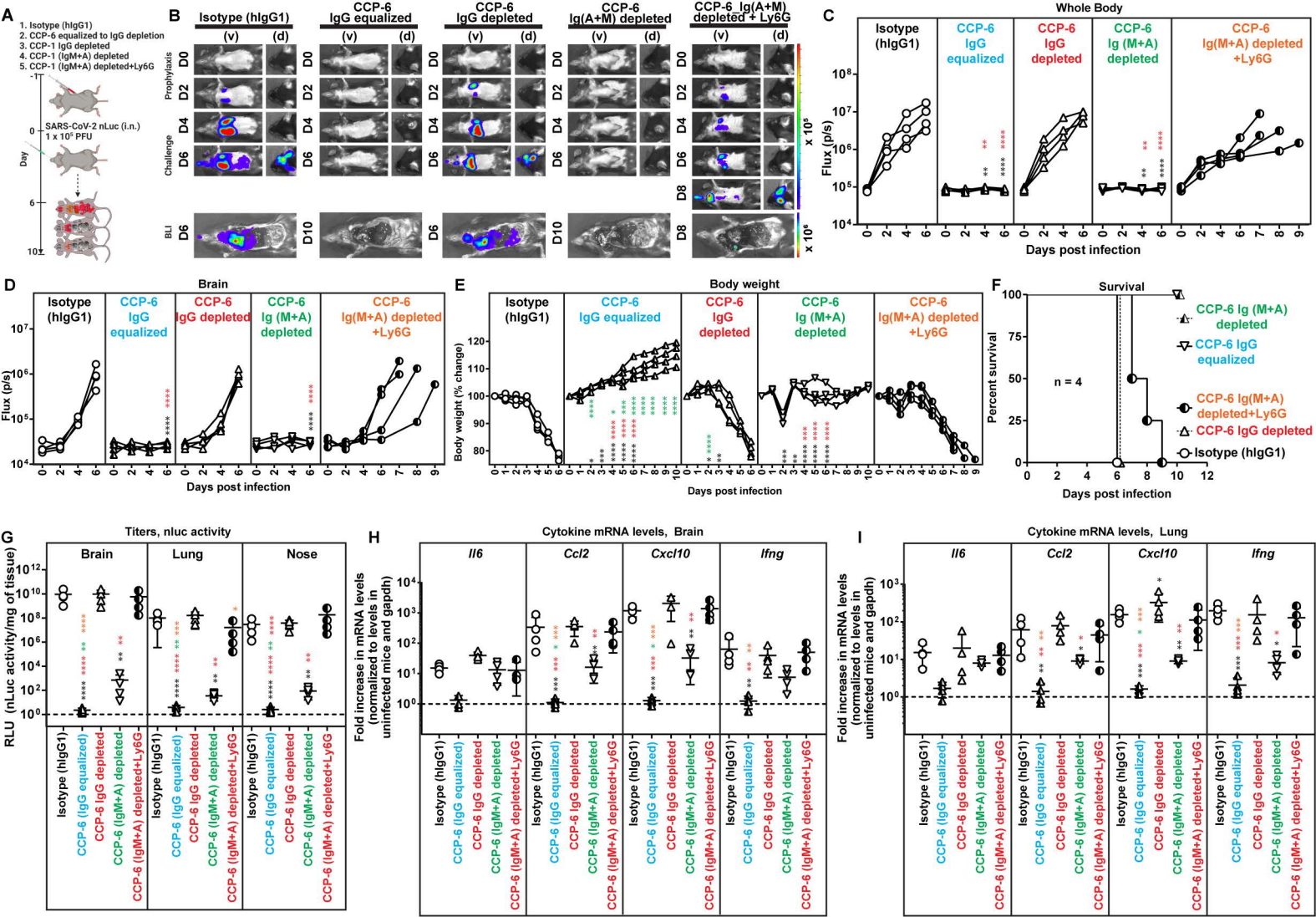
A
1. Isotype (hIgG1)
2. CCP-6 equalized to IgG depletion
3. CCP-1 IgG depleted
4. CCP-1 (IgM+A) depleted
5. CCP-1 (IgM+A) depleted+Ly6G
SARS-CoV-2 nLuc (i.n.)
1 x 10^5 PFU
Day
B
Isotype (hIgG1)
CCP-6 IgG equalized
CCP-6 IgG depleted
CCP-6 Ig(A+M) depleted
CCP-6 Ig(A+M) depleted + Ly6G
(v)
(d)
Prophylaxis
Challenge
BLI
C
Whole Body
Isotype (hIgG1)
CCP-6 IgG equalized
CCP-6 IgG depleted
CCP-6 Ig (M+A) depleted
CCP-6 Ig(M+A) depleted +Ly6G
Flux (p/s)
Days post infection
D
Brain
E
Body weight
Body weight (% change)
F
Survival
Percent survival
n = 4
CCP-6 Ig (M+A) depleted
CCP-6 IgG equalized
CCP-6 Ig(M+A) depleted+Ly6G
CCP-6 IgG depleted
Isotype (hIgG1)
G
Titers, nluc activity
Brain
Lung
Nose
RLU (nLuc activity/mg of tissue)
H
Cytokine mRNA levels, Brain
Il6
Ccl2
Cxcl10
Ifng
Fold increase in mRNA levels (normalized to levels in uninfected mice and gapdh)
I
Cytokine mRNA levels, Lung

Figure 6

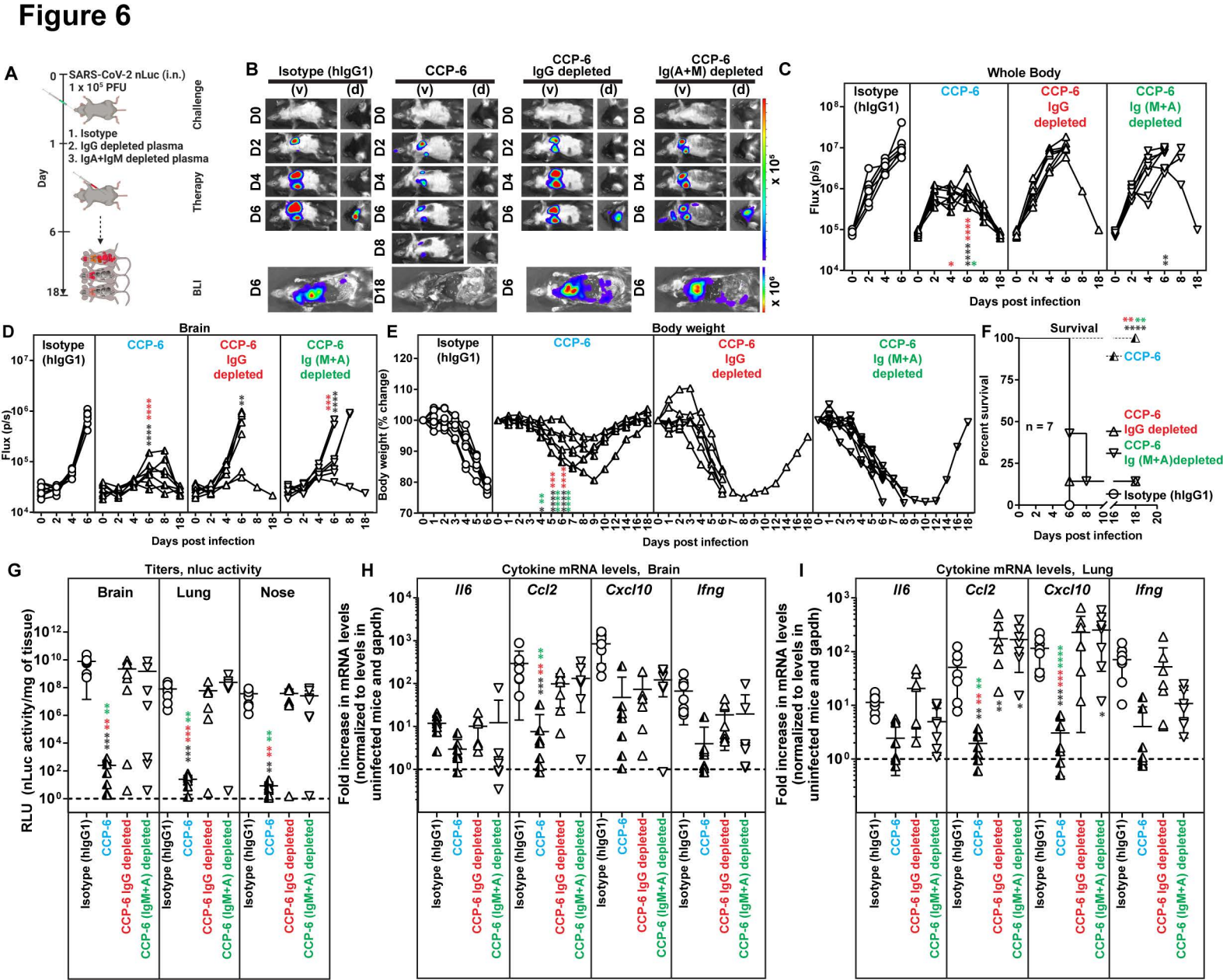
A
SARS-CoV-2 nLuc (i.n.)
1 x 10^5 PFU
1. Isotype
2. IgG depleted plasma
3. IgA+IgM depleted plasma
Day
Challenge
Therapy
BLI
B
Isotype (hIgG1)
CCP-6
CCP-6 IgG depleted
CCP-6 Ig(A+M) depleted
(v)
(d)
x 10^5
x 10^6
C
Whole Body
Flux (p/s)
Days post infection
D
Brain
E
Body weight
Body weight (% change)
F
Survival
Percent survival
n = 7
CCP-6 IgG depleted
CCP-6 Ig (M+A)depleted
G
Titers, nluc activity
Brain
Lung
Nose
RLU (nLuc activity/mg of tissue)
H
Cytokine mRNA levels, Brain
Il6
Ccl2
Cxcl10
Ifng
Fold increase in mRNA levels (normalized to levels in uninfected mice and gapdh)
I
Cytokine mRNA levels, Lung

Figure 7

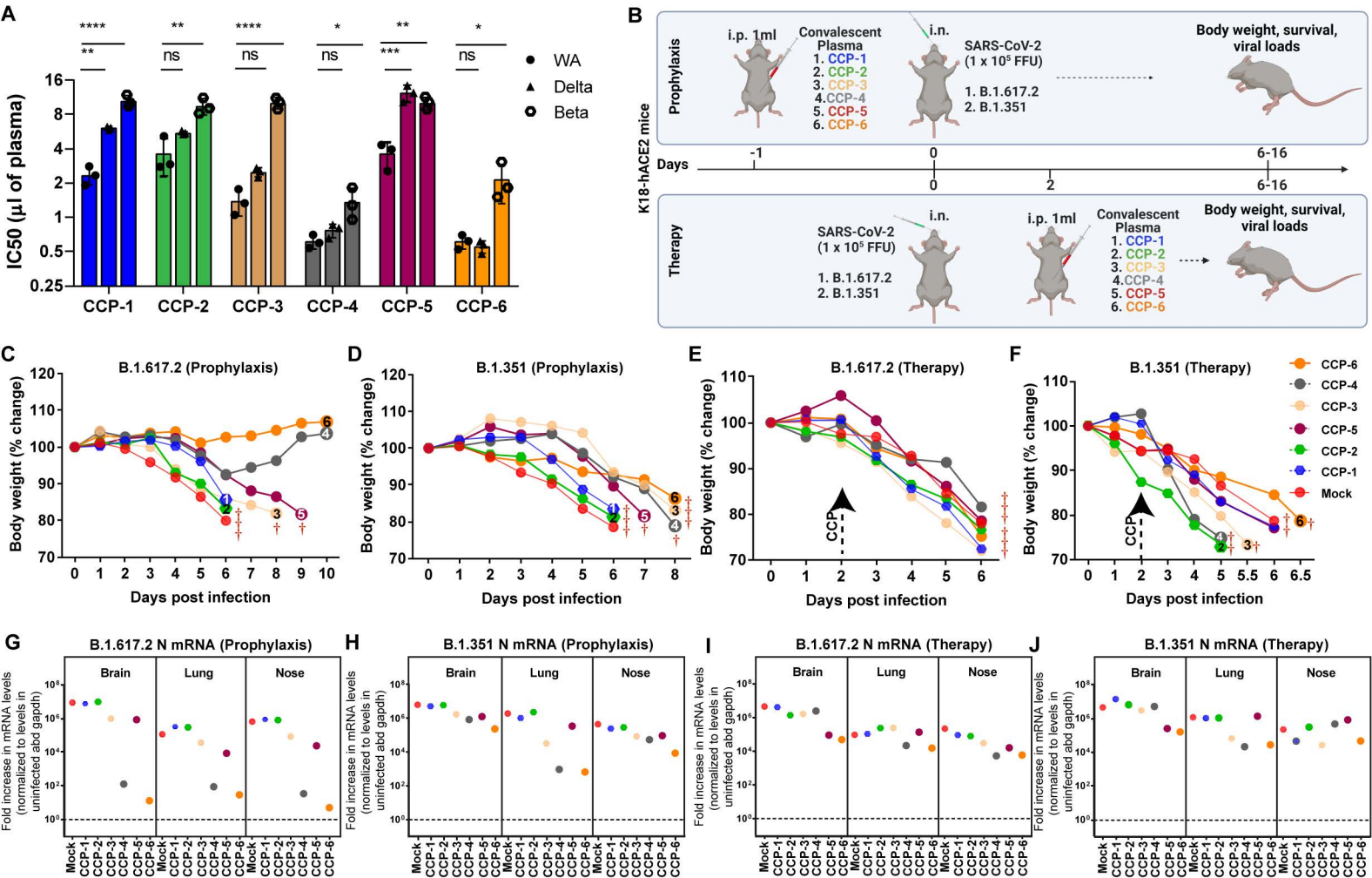
A
IC50 (µl of plasma)
WA
Delta
Beta
CCP-1
CCP-2
CCP-3
CCP-4
CCP-5
CCP-6
B
K18-hACE2 mice
Prophylaxis
i.p. 1ml
Convalescent Plasma
1. CCP-1
2. CCP-2
3. CCP-3
4.CCP-4
5. CCP-5
6. CCP-6
i.n.
SARS-CoV-2 (1 x 10⁵ FFU)
1. B.1.617.2
2. B.1.351
Body weight, survival, viral loads
Days
Therapy
C
B.1.617.2 (Prophylaxis)
D
B.1.351 (Prophylaxis)
E
B.1.617.2 (Therapy)
F
B.1.351 (Therapy)
Body weight (% change)
Days post infection
CCP
Mock
G
B.1.617.2 N mRNA (Prophylaxis)
H
B.1.351 N mRNA (Prophylaxis)
I
B.1.617.2 N mRNA (Therapy)
J
B.1.351 N mRNA (Therapy)
Brain
Lung
Nose
Fold increase in mRNA levels (normalized to levels in uninfected abd gapdh)